Silver nanoparticles loaded triple-layered cellulose-acetate based multifunctional dressing for wound healing

Shailesh Dugam[1], Ratnesh Jain[2]*, Prajakta Dandekar[1]*,

[1] *Department of Pharmaceutical sciences and technology, Institute of Chemical Technology, Mumbai*

[2] *Department of Biological sciences and biotechnology, Institute of Chemical Technology, Mumbai.*

Corresponding author's email address: <u>pd.jain@ictmumbai.edu.in</u>, <u>rd.jain@ictmumbai.edu.in</u>

Keywords:
Biopolymers, Electrospinning, nanofiber, bandage, antibacterial, wound healing

Abstract:
Chronic wounds present considerable challenges that delay their effective healing. Currently, there are several biomaterial-based wound dressings available for healing diverse wound types. However, most commercial wound dressings are too expensive to be affordable to patients from the middle and lower socioeconomic strata. Thus, in this investigation, affordable triple-layered nanofibrous bandages were fabricated using the layer-by-layer approach. The topmost layer comprises a hydrophilic polyvinyl alcohol layer, cross-linked with citric acid. The middle layer comprising cellulose acetate was loaded with silver nanoparticles as an antibacterial agent, while the lowermost layer was fabricated using hydrophobic polycaprolactone. The triple-layered nanofibrous bandages having a nano-topography, exhibited a smooth, uniform, and bead-free morphology, with the nanofiber diameter ranging between 200-300nm. The nanofibers demonstrated excellent wettability, slow *in vitro* degradation, controlled release of nano-silver, and potent antibacterial activity against Gram-negative *(E.coli)* and Gram-positive (*S. aureus*) bacteria. The fabricated bandages had excellent mechanical strength upto 12.72 ±0.790 M. Pa, which was suitable for biomedical and tissue engineering applications. The hemostatic activity of fabricated dressing has been investigated by thrombin-antithrombin (TAT), ELISA assay, moreover, the safety and proliferation capability have been evaluated using, 3-(4,5-dimethylthiazol-2-yl)-2,5-diphenyltetrazolium bromide (MTT) and EZ blue assay using human dermal fibroblast (HDF) and human keratinocytes (HeCAT) cell lines. The bandage demonstrated excellent *in vitro* hemocompatibility and biocompatibility. *In-vivo* excisional wound contraction, along with H and E and Masson's Trichrome staining further confirmed the potential of the nanofibrous bandage for full-thickness wound healing. Pre-clinical investigations thus indicated the possibility of further evaluating the triple-layered nanofibrous dressing in clinical settings.

1.0 Introduction

The skin plays an imperative role in protecting the body from microbes, radiations, thermal, biological and mechanical assaults and maintaining its physicochemical functions [1, 2]. However, the structural hallmarks and functions of the skin can be affected due to external factors such as cuts, burns, surgery, physical forces, chemical-induced damage, and metabolic

44 disorders like diabetes, which may induce wounds [3] [4]. The complex process of wound
45 healing comprises of various stages like coagulation and homeostasis, inflammation,
46 migration, proliferation and maturation [5]. However, any hinderance occurring during the
47 wound healing process leads to the development of chronic wounds. The complexity of
48 pathological and physiological conditions, in case of chronic wounds, complicates complete
49 skin regeneration, sometimes leading to massive infections and amputations in patients [1].
50
51 Currently, diverse types of wound dressings are commercially available to treat various wound
52 types. The conventionally available wound dressings like foam, and gauze which adsorb fluids
53 and exudates from the wound area, without keeping the wound moist. This leads to their
54 adherence to the wound and results in pain during their removal [5]. On the other hand, wound
55 dressings prepared from sodium hypochlorite and hydrogen peroxide, in the form of soaks,
56 normally act only as a temporary barriers for haemostasis and prevention of infections [5].
57 Thus, to overcome these limitations of the traditional wound dressings, various delivery
58 systems have been previously explored, which include hydrogels and hydrocolloids. [2, 6].
59 The hydrocolloids are generally useful for managing acute and chronic paediatric wounds, to
60 promote faster healing. However, the hydrogel-based dressings contain significant amount of
61 water and hence cannot adsorb large amounts of exudates and are thus applicable for low
62 exuding wounds. Additionally, these possess handling limitations due to their low mechanical
63 strength [2, 6]. Henceforth, in the last decade, natural and synthetic skin grafts have been
64 employed for skin regeneration [7]. However, due to high cost, requirement of expertise and
65 extensive care during handling and the inability to retrieve the original skin structure,
66 treatments with the grafts is largely limited. Thus, there is an urgent need to develop a
67 multifunctional wound dressing, that may be efficacious yet cost-effective than the existing
68 dressings, which was the focus of this study.
69
70 An ideal wound dressing, should be able to provide a moist environment, allow adequate gas
71 exchange, adsorb excess exudates and blood at the wound site, prevent wounds from bacterial
72 infections, allow painless removal, and should be easy to apply, non-toxic, non -allergic, should
73 have significant mechanical strength and be able to promote cell proliferation and migration to
74 accelerate the wound healing process [8].Thus owing to this prerequisite required for ideal
75 wound dressing , researchers have been focusing on the use of nanotechnology for fabricating
76 innovative wound dressings. Some of the nanosystems that have been reported as useful
77 include liposomes, carbon or quantum dots, carbon nanotubes, silver and gold nanoparticles,
78 dendrimers and nanofibers etc [9]. Nanofiber-based interventions have gained worldwide
79 attention due to their unique properties like small pore size, high pore volume, high drug
80 payload, high encapsulation efficacy, low density, high surface area-to-volume ratio for
81 solvation and release of drugs and functional molecules [10]. A number of approaches have
82 been adopted for the fabrication of nanofibers, like self-assembly, template synthesis, and
83 electrospinning etc. However, researchers have inferred electrospinning as a versatile
84 technique for fabrication of nanofibers due to the ease of application, high chances of
85 scalability, ability to use wide range of materials and tune their physicochemical properties as
86 nanofibers [11]. A wide range of synthetic, semi-synthesis, natural polymeric materials, either
87 alone or in combination, have been explored for the fabrication of electrospun nanofibers [12].

88 The mesh-like fibre structure of electrospun nanofibers promotes cellular adhesion, cell
89 proliferation, cell respiration, moisture retention, removal of exudates and haemostasis [13] .
90 Their high surface area-to-volume ratio, along with a matrix structure, allows tailored release
91 of encapsulated antimicrobial and therapeutic agents [14]. Additionally, small pore size and
92 large surface area governs better fluid absorption and greater oxygen permeability. The porous
93 nature of electropsun nanofibers prevents the tissue from dehydration, maintaining adequate
94 moisture at the wound site. Nanofibrous mats also provide significant physical and mechanical
95 protection to the skin [15]. Thus, electrospun nanofibers are able to provide all the essential
96 requirements for wound healing and hence are considered as potential candidates for wound
97 healing. Earlier, single layered electrospun nanofiber dressing, incorporating anti-bacterial
98 agents, was investigated for wound healing properties. Muhammad Qamar Khan et al,
99 investigated silver sulfadiazine loaded cellulose acetate nanofibers for burn-related wounds.
100 These nanofibers had a smooth and uniform morphology and exhibited significant antibacterial
101 activity, along with the desired physicochemical and structural properties for wound healing
102 [16]. However, single-layered nanofibrous dressing required frequent changing due to
103 excessive exudate absorption in the case of chronic wounds, which was especially painful for
104 the older people [17]. Additionally, due to the inability of single layered sheets to mimic the
105 behaviour of extracellular matrix, multi-layered nanofiber dressings attracted much attention
106 [18]. Layer-by-layer electrospinning approach has been widely accepted for fabrication of
107 multi-layered dressing. Here, one layer was electrospun at a time, which acted as the base for
108 the next layer that was electrospun over it. Serdar Torta et al. fabricated tri-layered nanofibrous
109 dressing wherein, the first and second layers were fabricated using alginate and chitosan. The
110 third co-axial layer consisted of collagen/PCL at the core and doxycycline in polyethylene
111 oxide as the shell. The developed wound dressing comprised of aligned nanofibers, which
112 exhibited a bio-adhesion value of 0.485 mJ/cm^2 over the rat skin, an excellent tensile strength
113 of 2.76 MPa, and a porosity of 52.3 %, with good wettability and no cytotoxic effect towards
114 the keratinocytes. Thus, the three-layered wound dressing acted as good intervention for
115 wound healing applications. [19]. However, application of these dressing restricted due to the
116 risks associated with the pathogen transmission, which varied with the collagen source and
117 enzymatic degradation of collagen, ultimately leading to a lower dressing stability [20, 21].
118 Thus, there is need to develop alternative multi-layered wound dressing.
119
120 In this investigation, we have fabricated a triple-layered electrospun nanofiber bandage using
121 the layer- by-layer approach, wherein, top layer fabricated using PVA and crosslinked with
122 citric acid, middle layer of CEA with inclusion of AgNPs and basal layer with hydrophobic
123 PCL. The topmost layer was fabricated using poly vinyl alcohol (PVA) due to its versatile
124 properties, relatively low cost, large availability, significant solubility in aqueous solutions,
125 ability to prevent dehydration and excellent mechanical strength [22]. However, to achieve a
126 slow degradation and to improve its mechanical strength, this layer was cross-linked with the
127 green crosslinker, citric acid (CA). The use of CA to crosslinked PVA layer not only improve
128 the stability of PVA layer it will also   provide the acidic condition at wound site which helps
129 to alter protease activity in the wound area and lead to detoxification of its toxic end products.
130 Moreover, acidic pH will also enhance the flux of oxygen within the wound niche and
131 accelerate healing rate. In addition to this, use of citric acid has been projected to promote re-

epithelialisation and angiogenesis (due to enhanced oxygen uptake) which will result in faster formation of healthy granulation tissue and hence rapid healing of wound [23] .The middle layer consisted of cellulose acetate (CEA) and incorporated the silver nanoparticles (AgNPs) as an anti-bacterial agent. CEA due to its excellent biocompatibility, slow biodegradability, a high thermal stability, coagulation properties water absorption abilities, regenerative potential and thus exudate adsorption and ability to interact with the skin cells [24]. However, poor antibacterial activity and low mechanical strength limit its application. Thus, inclusion of AgNPs and the mechanical support provided by the overlying PVA layer improved the functional properties of the CEA layer. The presence of free radicals and bacteria leads to harmful cytotoxic effects, triggers oxidative stress and delays the wound healing process [25]. Therefore, the use of an appropriate antibacterial and antioxidant agent may be an important strategy to improve wound healing by reducing excess free radicals and persistent inflammation. AgNPs with ability to oxidise into aqueous environment and able to provide broad range antibacterial effect for prolonged period of time through slow release of silver nanoparticle from polymeric matrix assess the wound healing process. Finally, the basal layer was fabricated using the hydrophobic polycaprolactone (PCL) to achieve a good adhesion to the skin cells and avoid the painful removal of the bandage. Also, the porous structure of the PCL layer mimicked the extracellular matrix of the skin and provided significant oxygen permeability, for effective wound healing [26, 27]. Moreover, each of these layers was synthesized using widely and commercially available polymers, that are well accepted in the pharmaceutical industry, using a scalable and commercially feasible manufacturing process. Thus, considering the unique properties of these electrospun layers, each having a nano-topography, we hypothesized that the unique PVA/CEA/ PCL multi-layered dressing, containing AgNPs, could collectively provide an effective, wound-healing solution.

2.0 Objectives
1. To Design and develop a multi-layered wound healing dressing
2. To optimize of physicochemical properties of the wound healing bandage
3. To perform Cellular evaluation of the wound healing bandage for cytotoxicity and antimicrobial activity
4. To investigate the wound healing efficacy of developed dressing by preclinical studies

3.0 Materials and Methods
3.1. Materials
Cold water soluble PVA (MW ~ 160000 g/mol; degree of hydrolysis ~ 86.50-89 mol %) was purchased from Himedia Laboratories Pvt. Ltd., Mumbai, India. Cellulose acetate CEA (MW ~ 30000 g/mol) was purchased from Sigma Aldrich Ltd. (USA), polycaprolactone PCL (MW ~ 80000 g/mol) was purchased from Sigma Aldrich Ltd. (USA), dimethyl sulphoxide (DMSO) analytical grade (AN) , N, N dimethyl formamide (DMF) AR grade, methanol, tetrahydrofuran (THF), acetone, chloroform AR grade, ethylene diamine tetra acetic acid dipotassium salt LR grade (EDTA), citric acid (CA) were purchased from SD Fine Chemical Limited, Mumbai. Silver nitrate (AgNO$_3$, MW ~169.87g/mol) and sodium borohydride (NaBH$_4$,MW ~ 37.83) was purchased from Avra synthesis, Hyderabad (India), *Escherichia Coli* ATCC 25922 and *staphylococcus aureus* ATCC 25923 were obtained as gift samples from Khalsa college,

176 Mumbai (India). Nutrient broth (N.B.), agar−agar, Dulbecco's Modified Eagle Medium
177 (DMEM), human dermal fibroblast (HDF) cell line, 3-(4,5-dimethylthiazol-2-yl)-2,5-
178 diphenyltetrazolium bromide (MTT) and EZ Blue cell assay kit were obtained from Himedia
179 Laboratories Pvt. Ltd., Mumbai, India. Fetal bovine serum (FBS) was procured from
180 Invitrogen, USA, while 1% antibiotic-antimycotic was from Life Technologies, Mumbai.
181 Human ELISA kit –TAT was acquired from (Biogenuix medystem, India). The human
182 keratinocyte (HaCaT) cell line was kindly gifted by ACTREC, Mumbai, India. Deionized and
183 double-distilled water (Milli-Q Plus system, Millipore, Bedford, MA, USA) was used in all the
184 experiments. The electrospinning unit, EspinNano-2, was purchased from Physics equipment,
185 Chennai, India
186
187 **3.2 Fabrication of PVA nanofibers as the top layer and its cross-liking with citric acid**
188 PVA nanofibers were fabricated as per a previously reported method, with slight modifications,
189 as needed [28]. Initially, 9% w/v of PVA was dissolved in distilled water by continuous stirring
190 for 4 h, till a homogenous solution was obtained. Further, the homogenous solution was loaded
191 into a 5mL of syringe, fitted with a 18 G needle, and the nanofibers were electropsun using
192 optimized electrospinning process parameters. The flow rate was maintained at 1mL/h, voltage
193 at 20 kV, while the distance between the collector drum and the tip of the needle was kept at
194 10 cm, at the temperature of 30 ± 2 ℃ and relative humidity range of $40\% \pm 2\%$ to $60\% \pm 2\%$.
195 The nanofibers were collected over a collector drum, on an aluminium foil. The layered
196 nanofibrous sheet was peeled off and further cross-linked using citric acid (CA). The
197 nanofibrous mats was cross-linked with various weight percentages of CA, ranging from 1 %
198 to 5 % (w/v), to enhance their mechanical property. The cross-linked nanofibrous mats were
199 treated in vacuum oven with vapours of CA, at 90°C, for 15 min. Here, the heat treatment was
200 crucial to complete the cross-linking process [29]. The cross-linked nanofibrous sheets were
201 then used for further characterization
202
203 **3.3. Fabrication of silver nanoparticle loaded (AgNPs) CEA nanofibers as the middle**
204 **layer:**
205 Initially, AgNPs were synthesized in-house using a unique micellar technology, based on the
206 chemical reduction of 10mM of silver nitrate ($AgNO_3$) using 3mM of sodium borohydride
207 ($NaBH_4$). Here, $NaBH_4$ was used as the reducing agent while poly ethylene glycol (PEG) was
208 used as the capping agent. The method for formulation for AgNPs was optimized with respect
209 to process parameters like the residence time (sec), flow rate of the $AgNO_3$ solution (µL/min),
210 flow rate of the $NaBH_4$ solution (µL/min), flow ratio of the $AgNO_3$ and $NaBH_4$ and the
211 concentration of the capping agent. The detailed optimization protocol and methods for the
212 characterization of silver nanoparticles have been described in the supporting information.
213 The prepared silver nanoparticles then dispersed in water at concentration 200ppm. Then, the
214 prepared AgNPs dispersion added in dropwise manner into polymeric solution of cellulose
215 acetate (CEA, 16% w/v) solution in dimethylformamide (DMF) and acetone, at the ratio of 1:
216 3 v/v with continuous stirring at 500rpm to get homogenous solution of CEA with
217 incorporation of AgNPs.
218 The AgNPs loaded CEA nanofibers were fabricated by slightly modifying a previously
219 described electrospinning protocol [16]. The dispersion of AgNPs in water, at the

concentration of 200 ppm, was mixed with the CEA solution in DMF (16% w/v) and acetone, at the ratio of 1: 3 v/v. Further, this mixture was filled into 5 mL syringe, fitted with 18 G needle, and the solution was electropsun over the previously collected PVA layer. The optimized electrospinning parameters included a voltage of 16kV, flow rate of 0.7mL/h and the distance between collector drum and tip of needle of 10cm, the temperature of 30 ± 2 ◦C and relative humidity range between 40% $\pm$ 2% to 60% $\pm$ 2%. The developed sheet was used for further characterization.

3.4 Fabrication of polycaprolactone nanofiber as the lower layer

Porous PCL layer was fabricated by modifying a previously reported electrospinning method based on non-solvent induced phase separation mechanism (NIPS) [30]. Initially, PCL was dissolved at the concentration of 10% w/v in a mixture of chloroform and dimethyl sulfoxide, at the volume ratio of 3:1 (good/bad solvent), at 25 °C. This solution was fed into 5 mL syringes, fitted with 18 G needle, and the solution was electrospun on formerly collected CEA layer. The optimized parameters for the electrospinning process was flow rate of 1 mL/h, voltage of 20 kV, syringe tip-to-collector distance of 10 cm, temperature of 30 ± 2 °C and relative humidity range of 40% $\pm$ 2% to 60% $\pm$ 2%. The fabricated matrices were peeled off and used for further characterization.

3.5 Morphological evaluation using SEM and TEM

Morphological analysis of the electropsun, non-crosslinked (PVA NFs) and crosslinked PVA nanofibers (PVA CA NF), CEA nanofibers (CEA NF) and PCL nanofibers (PCL NF), individually, and as cross-section of AgNPs loaded the triple layered nanofibrous sheet (TNF) was conducted after sputtering with gold coating (Denton gold sputter unit for 120 s). A field emission electron microscope (FEI Quanta 2000, Netherlands) operating at a 10 kV acceleration voltage was used for the analysis. Using ImageJ software, the average diameter of the nanofibers (n = 50) was determined. The CEA electropsun nanofibers loaded with AgNPs were first submerged in acetone. The separated nanofibers were next seen in transmission electron mode (FEI Tecnai 12, Netherlands) at an acceleration voltage of 200 kV for ten minutes on a carbon-coated TEM grid.

3.6 Attenuated total reflectance infrared spectroscopy (ATR-FTIR)

To comprehend any potential chemical interactions between the polymers or the creation of ester bonds during cross-linking, structural investigation has been performed using by Attenuated Total Reflectance Fourier Transform Infrared Spectroscopy (ATR FTIR, JASCO FT/IR- 4000). The spectra were obtained between the wave numbers 400 to 4000 cm^{-1}

3.7 Thermo Gravimetric Analysis (TGA) of the TNF

Thermo gravimetric analyses of PVA, PVA NF, CA, PVA CA NF, CEA, CEA NF, PCL, PCL NFs, and TNF were performed to study their thermal behaviour and decomposition temperature. The investigations were carried out utilizing a thermogravimetric/differential thermal analysis (TGA/DTA) device (DTG-60H SHIMADZU, Japan), which was capable of measuring both simultaneously. All the samples were analysed in the temperature range of 30

263   –600 °C, at the heating rate of 10 °C/min, in a nitrogen atmosphere, at the flow rate of
264   100mL/min.

265

266

267   **3.8 Crystal structure elucidation by X-ray diffraction (XRD)**
268   The X-ray diffraction patterns of PVA, PVA NF, CA, PVA CA NF, CEA, CEA NF, PCL, PCL
269   NF, and TNF sheets were recorded using (Lab X XRD-6100 SHIMADZU, Japan), equipped
270   with Cu Kα radiation (λ = 1.54 Å. The XRD patterns were characterized in the 2θ range of 5–
271   50°, with a step size of 0.02° and a counting time of 5s/step. The generator voltage was
272   maintained at 40 kV, and the generator current was 30 mA.

273

274   **3.9 Water uptake study**
275   During the water uptake study, the PVA CA NF, CEA NF, PCL NF and TNFs, weighing 20-30
276   mg, were immersed in 10 mL of 1X phosphate buffer saline (PBS), over a period of 7 to 15
277   days. The mats were immersed separate in glass vials [31]. The water uptake of the NFs was
278   calculated on the basis of wet and dry weights using Equation (1). The excess water from the
279   mats was removed with a filter paper, before calculating the water uptake. All the measurement
280   was recorded in triplicates (n=3)

281   $$Water\ upake\ ability = \frac{(Wf-Wi)}{Wi} * 100\% \qquad \text{Equation (1)}$$

282   where, Wi represented the initial dry weight of the nanofibrous mats and Wf represented the
283   wet weight of the nanofibrous

284

285   **3.10 Water vapor transmission rate**
286   The water vapor transmission rate (WVTR) was measured using the rate of change of mass of
287   water in the vials. The PVA CA NF, CEA NF, CEA AgNPs NF, PCL NF and TNF sheets were
288   cut into pieces having dimension of 3 cm x 3 cm and thereafter were mounted on the mouth of
289   a cylindrical glass vial containing distilled water. The vials with samples were sealed using a
290   paraffin tape and then placed in an incubator, at 50% relative humidity. The weight change of
291   water was measured manually, at the interval of 24 h and the WVTR was calculated using
292   Equation (2). The initial weights of the vials were recorded and the final weights were measured
293   after 24 h. All the measurements were recorded in triplicates (n = 3).

294   $$Moisture\ upatke = \Delta W\ A \qquad \text{Equation (2)}$$

295   where, ΔW was the difference in initial and final weight (g) of the water in the glass vials, A
296   was the surface area exposed (m2) for 24 h and WVT was expresses as g/m^2 /day [32]

297

298   **3.11 Porosity evaluation**
299   The porosity of the PVA CA NF, CEA NF, CEA AgNPs NF,PCL NF and TNF sheets was
300   measured by the liquid displacement method [33]. The samples mentioned above absorb ethanol
301   without becoming swollen. The each mat were submerged for 5 min in a known volume of
302   ethanol (v1) within a graduated cylinder. The entire volume of ethanol that penetrated the NFs
303   sheets was then recorded as volume (v2). After removing the ethanol-penetrated nanofiber mats
304   from the cylinder, the quantities of ethanol that remained were noted (v3). Equation (3) was
305   utilized in the computation of porosity.

306

$$\% \ Porosity \ = \frac{V1-V3}{V2-V3} * 100 \qquad \qquad \text{Equation (3)}$$

3.12 Water contact angle measurement

Water loving and hating properties of the PVA CA NF, CEA NF, PCL NF and TNF sheets were measured using KYOWA interFAce Measurement and Analysis System- FAMAS. The samples were placed on the stage, following which a droplet of deionized water (2 µL) was placed on the surface of the sample. The image of water droplet on each sample was captured and the contact angles were measured by using ImageJ program.

3.13 Mechanical strength analysis

The tensile strength of the nanofibrous mats was studied using a Electroforce 5500 model (TA, instruments USA). For determination of the mechanical strength for non-crosslinked, and crosslinked PVA NF, CEA NF, AgNPs loaded CEA NFs and PCL NF, individually, and the TNFs. The 3 cm x 3 cm nanofibrous mats were put in the sample holder, and the force at which the mats began to deform was measured as well as the tensile strength at room temperature (25 °C) under a load of 20 N and a crosshead speed of 50 mm/sec. The mechanical strength of nanofibrous mats were calculated using Equation (4).

$$Mechanical \ strength = \frac{Force \ required \ to \ break \ the \ sheet}{cross \ sectional \ of \ sheet} \quad \text{Equation (4)}$$

3.14 *In vitro* degradation studies of the nanofibrous mats

After calculating the initial weight of the mats, degradation tests of PVA CA NF, CEA NF, CEA AgNPs NF, PCL NF, and TNF were conducted. The mats were then incubated at 37°C with 10 mL of phosphate buffer saline (pH 7.4) containing lysozyme (0.25 mg/mL, 10000U/mL). The concentration of the enzyme that was utilized was comparable to that of human serum. [34]. In order to retain mat activity, 10 mL of fresh lysozyme was introduced every 3 days. After that, the samples were mixed with 0.2 mL of 0.25 M EDTA to inactivate any remaining lysozyme. The samples were taken out at the conclusion of each degradation period, freeze-dried, and cleaned three times using distilled water in order to determine the weight loss. Equation (5) was used to compute the weight reduction.

$$\% \ weight \ loss = \frac{Wi-Wf}{Wf} * 100 \qquad \qquad \text{Equation (5)}$$

where, Wi is the initial weight of the samples and Wf is the final weight of the samples.

3.15 Evaluation of cellular toxicity using MTT assay

The cellular cytotoxicity of PVA CA NF, CEA NF, CEA AgNPs NF,PCL NF and TNF mats were evaluated to confirm their safety towards the human dermal fibroblasts (HDF) and human keratinocyte cells (HaCaT) using the MTT assay [35] . The cells were cultured in a 24-well plate, in DMEM F12 medium, supplemented with 10% fetal bovine serum(FBS) and 1% antibiotic-antimycotic solution. The medium was changed every 72 to 96 hours. After trypsinizing the cells, an automatic cell counter (Countless 3FL, Invitrogen India) was used to count the number of cells. Following a 5 min centrifugation at 20 ºC, the resultant cell suspension was again suspended in the enriched medium. For the MTT assay, all the non-

349 crosslinked and crosslinked PVA NF, CEA NF and PCL NF, individually, and the TNF sheet
350 were sterilized using ethylene oxide sterilization (gas concentration used -90% ethylene oxide
351 and 10% CO_2, temperature -60°C and time 6h).The 20 mm × 20 mm nanofibrous sheets were
352 seeded with 3 x 10^5 cells in 2 mL of the supplemented media, and they were then incubated for
353 24 hours at 37°C, with 5% CO2 and 99% relative humidity. Incubation took place for 4 hours
354 after the old medium was removed from the wells and replaced with 2 mL of fresh medium,
355 wherein 500 μL of the MTT reagent were added. Under a microscope, formazan crystal growth
356 was seen. After dissolving the formazan crystals in each well with 500 μL of cell culture grade
357 DMSO, the absorbance was measured at 570 nm, with the background absorbance measured at
358 690 nm, using a multimode microplate reader (VICTOR® Nivo™ PerkinElmer, Singapore).
359 Relative % cellular viability was calculated by Equation (6).
360
361 $$\% \, cell \, viability = \frac{(\,A570-690) \, cells \, treaed \, with \, NF \, sheet}{(\,A570-A690) \, control \, cells} * 100 \qquad \text{Equation (6)}$$
362
363
3.16 Cellular proliferation study using EZ blue assay
365 The cellular proliferation over the PVA CA NF, CEA NF, CEA AgNPs NF,PCL NF and TNF
366 mats were evaluated using the human dermal fibroblast (HDF) and human keratinocyte cells
367 (HaCaT), using the Alamar blue assay [36]. The cells were cultured in a 24-well plate, in
368 DMEM F12 supplemented with 10% fetal bovine serum (FBS) and 1% antibiotic-antimycotic
369 solution. The medium was replaced every 72 to 96 h. The cells were trypsinized and the cell
370 count was measured using an automated cell counter (Countless 3FL, Invitrogen India). The
371 resulting cell suspension was centrifuged for 5 min, at 20 °C, and re-suspended in the
372 supplemented medium. For the EZ blue assay, all the non-crosslinked and crosslinked PVA
373 CA NF, CEA NF, CEA AgNPs NF,PCL NF and TNF mats were sterilized ethylene oxide
374 sterilization (gas concentration used -90% ethylene oxide and 10% CO_2, temperature -60°C
375 and time 6h). The nanofibrous sheets having the dimension of 20 mm x 20 mm were seeded
376 with cells, at the density of $3x10^5$ cells in 2mL of the supplemented medium and incubated at
377 37 °C, in presence of 5% CO_2 and 99% relative humidity. The constructs were evaluated using
378 EZ Blue assay on days 1, 2 and 3. The media was replaced with 2 mL of fresh medium
379 containing 10% EZ Blue dye (10% EZ Blue blue, 80% medium and 10% FBS v/v) and
380 incubated for 3h. Later, 300 mL of the medium was pipetted out to measure the absorbance at
381 the wavelength of 570 nm, keeping 600 nm as the reference wavelength, in the microplate
382 reader (VICTOR® Nivo™ PerkinElmer, Singapore). The manufacturer's protocol was
383 followed to calculate the percent dye decrease which are a sign of cellular proliferation
384
3.17 Thrombin generation assay to assess the haemostasis activity
386 The thrombin generation assay was conducted using heparinized samples of whole human
387 blood obtained in EDTA coated 50 mL tubes. The samples PVA NF, PVA CA NF, CEA NF,
388 CEA AgNPs NF, PCL NF, and TNF mats in comparison with gauze were tested for thrombin
389 generation. One millilitre of blood was incubated on the sterile mats for one hour at 37 °C. To
390 prevent the creation of new thrombin, 0.3 mL of sodium citrate solution (0.633 M) was
391 combined with the blood sample. Next, the entire blood was separated from the plasma by

392 centrifuging it for 20 minutes at 28 °C at 4000 rpm. The plasma obtained was subjected to
393 further treatment to determine thrombin generation throughout 1h, using the thrombin-
394 antithrombin complex human ELISA kit TAT, as per the manufacturer's instructions
395
396 **3.18 Loading and release characteristics of AgNPs**
397 AgNPs were dispersed and added to the electrospinning solution for the CEA layer at a 200
398 ppm concentration. The precise concentration of silver (30 mg) in the form of Ag+ ions was
399 measured on a 3 cm × 3 cm CEA mat prior to the in vitro release tests. By dissolving the
400 samples in 95% nitric acid (HNO3; 5 mL) and adding the release medium (PBS, pH 7.4)
401 containing lysozyme (10,000 U/mL in PBS pH 7.4, 10 mL) to duplicate the presence of
402 enzymes in injured tissues, the amount of silver contained in CEA mat was ascertained. Using
403 0.1 N NaOH, the medium's pH was brought to neutral. The inductively coupled plasma atomic
404 emission spectroscopy (ICP-MS) was used to detect the concentration of liberated silver from
405 the TNF mat. [37]. Over 7 days, the quantity of silver released was measured at predetermined
406 intervals. Measurements were done in triplicate at each time point. The amount of silver
407 contained in the specimens before they were submerged in the release medium was used to
408 compute the cumulative silver release, which was determined after carefully analysing the data
409 that was collected. Equation (7) provides the formula for computing cumulative silver release.

410 $$Cumulative\ amount\ of\ silver\ relaese\ (\%) = \frac{Mt}{Mi} * 100 \quad \text{Equation 7}$$

411 where Mi was the quantity of silver in the samples prior to the release studies, and Mt was the
412 amount of silver released at time t. The release profile AgNPs from TNF was analysed by PCP-
413 Disso-V3.08 software. Here, to describe the dissolution pro-file in a model-dependent manner,
414 the zero-order, first-order, Higuchi, Hixson-Crowell, Korsmeyer, and Peppa's equations were
415 chosen. Three key factors were considered for the release mechanism study: the n-release
416 exponent, the k-release rate constant, and the r^2 correlation coefficient. [33]
417
418 **3.19 Antibacterial evaluation**
419 The disc diffusion method, were used to investigate the anti-bacterial activity of AgNPs
420 incorporated TNF against two common bacteria present in infected wounds, *Escherichia coli*
421 and *Staphylococcus aureus*, was evaluated in order to determine its potential utility as a
422 functional wound dressing. [38].*Staphylococcus aureus* ATCC 25923 and *Escherichia coli*
423 ATCC 25922 cultures were used to create the bacterial inoculums. The cultures were serially
424 diluted with peptone water after being cultured in nutrient broth for a whole night at 37 °C. The
425 prepared microbial suspensions were flooded onto petri plates that contained Nutrient Agar.
426 Microorganisms that had not been treated served as the negative control, whereas AgNP
427 dispersion (0.3 ppm) was employed as the positive control. After applying TNF (2 cm × 2 cm)
428 to the plate surface, it was incubated at 37 °C for a full day. The zone of inhibition in each plate
429 was measured in centimetres after incubation.
430
431 **3.20 *In-vivo* wound healing efficacy of the multi-layered nanofibrous mat**
432 This study aimed to compare the therapeutic efficacy of cotton gauze, a typical dressing, with
433 AgNPs laden TNF mats. In this work, the wound healing process was examined using the
434 partial thickness wound model in Sprague-Dawley rats. The Institutional Animal Ethics
435 Committee (IAEC) approved the acquisition of eighteen male Sprague-Dawley rats, which

were obtained from the National Institute of Biosciences in Pune (Approval No.: ICT/IAEC/2022/M02/P17). Each animal was kept in a separate plastic cage and given water and sterile rodent chow for food. The rats were given seven days to acclimate before the trials began. Rats were given intraperitoneal injections of ketamine-xylazine in an 80:20 v/v ratio, with a dose of 80 mg/kg ketamine and 20 mg/kg xylazine, to induce anaesthesia. Using a clipper, the hair was removed from the dorsal region of the rat, and fine hair was removed using a shaving razor and depilatory cream without causing any injury to the skin. Afterwards, surgical spirit was used to clean and disinfect the affected area. A total of six male Sprague Dawley rats were randomly assigned to three groups. The first group was used as a negative control, in which the wounds were left untreated. The second group was a positive control, in which cotton gauze treatment was applied. While, the third group was used as a test group, having TNF mats with AgNPs inserted over the rat skin. A partial thickness wound model in the dorsal region of the rat, with each wound having an 8 mm diameter, made with a sterile biopsy punch. Each rat's dorsal region was cleaned with diluted iodine, and the wounds were then dressed appropriately and secured with medical tape. Further dressing was changed on day 3, 7 and 10

3.21 Wound area measurement

The wound dressing was taken off on days 3, 7, and 10, and the areas of the wounds were measured using a clear polyethylene sheet. The region was marked with a marker pen and the sheet was left over the wound. The highlighted region was then moved to a graph sheet so that the precise measurements could be ascertained. The wound was photographed concurrently. Equation (8), based on the image, was used to compute the rate of wound healing and quantify the area of the wound using Image J software.

$$\% \ rate \ of \ woud \ healing = \frac{Awi - Awn}{Awi} * 100 \qquad \text{Equation (8)}$$

where,

Awi was the initial area of wound

Awn was the remaining area of wound on the nth day of wounding

3.22 Haematoxylin and eosin/ Masson's Trichrome staining

The damaged rat's skin was cut into 5*5 centimeter pieces on day 10. To stop the skin tissue from deteriorating, it was submerged in a 10% formalin solution. After that, tissue-embedding paraffin blocks were ready. The paraffin slices were placed on super freeze slides, dried on a hot plate, and then submerged in three sets of xylenes for ten minutes each to get ready for H&E staining. Following that, the object was cleaned with three sets of 100% ethanol for ten minutes each, and then it was rinsed with tap water. The portions had to be dehydrated and the wax removed. After five minutes in hematoxylin, the slides were carefully washed under tap water for a duration of roughly 4-5 minutes. After adding 1% acid alcohol (1% HCl in 70% v/v alcohol) for five seconds and washing with tap water, excess haematoxylin was eliminated. Scott's tap water was used to wash the pink haematoxylin stain for around ten seconds, or until the sections turned blue. After rinsing the slides in tap water, they were stained for 15 seconds with 1% w/v eosin and then rinsed for 1 to 5 minutes under running tap water. After that, the sections were dehydrated for ten minutes each using two washes of pure alcohol and two washes of xylene. Afterward, they were mounted in DPX mount and protected with glass cover

479 slips. After that, the slides were examined under a microscope. Additionally, Masson's
480 Trichrome staining was used to examine and quantify the expression of collagen in wound
481 tissues. The proportion of the wound that was blue was used to measure collagen expression
482

4.0 Statistical analysis
484 Statistical analysis was conducted by use of the Student's t-test approach and GraphPad Prism,
485 Windows version 8.2 (GraphPad Prism San Diego California USA), statistical analysis was
486 performed. The format of the data was mean ± standard deviation (SD). At the probability
487 level, P-values less than 0.05 were considered statistically significant, and those less than 0.001
488 were considered extremely significant.
489

5.0 Result and Discussion
**5.1. Standardisation of the electrospinning and the cross-linking methods**
492 The morphology of electrospun nanofibers depends on various properties of the polymeric
493 solutions, such as their viscosity, polymer concentration, conductivity and surface tension, as
494 well as various electrospinning process parameters, like voltage, flow rate, syringe translation
495 movement, and distance between the tip of the needle and the collector drum. All three layers,
496 viz. the topmost PVA layer, the middle CEA layer, and the bottom-PCL layer, were optimized
497 with respect to the polymeric solution characteristics and electrospinning paraments at which
498 uniform nanofibers were obtained. Since, PVA nanofibers, due to their inherent hydrophilic
499 properties, were rapidly degraded in aqueous solution, they were unbale to maintain their porous
500 structure. Thus, PVA NFs were further cross-linked to impart them water stability. A number
501 of approaches have been employed for cross-linking PVA, including formation of its blend with
502 hydrophobic polymers and the use of chemical cross-linkers. Various cross-linkers, like
503 glutaraldehyde [39], glyoxal [40], malic anhydride [41] etc. have been used for cross-linking
504 of PVA. However, these crosslinkers are toxic at higher concentrations and also do not offer
505 the required level of stability [42]. On the other hand, organic acids such as citric acid, are
506 biocompatible and can provide desired properties and improve the adhesion and proliferation
507 of cells [43]. In this study, cross-linking of PVA nano-mats was conducted using CA, at
508 different concentrations (1-5%w/v), along with thermal treatment. Further, the effect of cross-
509 linking on the morphology of PVA NF mats was studied using SEM. Also, cross-linking with
510 CA was confirmed using FTIR spectroscopy.

5.2 Morphological analysis using SEM and TEM
512 Morphological analyses of PVA NF, PVA CA NF, CEA AgNPs NF,PCL NF and TNF were
513 performed using SEM. Field emission electron microscopic images of different nanofibrous
514 layers and their diameter distributions have been presented in Figures 1 A-H. The individual
515 layers of the TNF dressing comprised of nano-ranged fibers, having uniform, smooth, and
516 bead-free structure. The average diameter of the PVA NF in the top layer of the TNF mats was
517 found to be 132.46 ± 15.32 nm (Figure 1 A). SEM images (Figure 1 B-D) showed that the
518 nanofiber mats, when cross-linked with 1-3% w/v citric acid, resulted in smooth and uniform
519 nanofibers, with slight bigger average fiber diameter as compared to the fibers in the non-cross-
520 linked mats. Further, upon increasing the concentration of the citric acid from 4-5 % w/v, it was
521 found that the fibers formed were thick, non-uniform, rough, and exhibited bead formation, as

seen in Figures 1E and 1F. Thus, the PVA NF mats were crosslinked with 3 % w/v of CA in all the further investigations. The nano-mats cross-linked with appropriate concentration of CA were able to preserve a web-like structure. The average diameter of the NFs in the CEA layer containing the AgNPs was found to be 161.23±12.23 nm, as seen in Figure G. While, Figure 1H, confirms that the average diameter of NFs in the PCL layer was 212.56. ±27.23 nm. It was anticipated that the web-like structure of the fabricated NF mats could help in significant cellular respiration and prevent the wound from being dehydrated Also, the structure suggested a high surface area-to-volume ratio, which was hypothesized to enable higher absorption of the wound exudates. Additionally, the AgNPs loaded CEA layer NFs were assessed using a transmission electron microscope, which confirmed the presence of AgNPs within the NFs, as shown in Figures 1 I-J. The sizes of the optimized AgNPs were analysed by TEM (Figure S2). Further, the loading of NPs was also confirmed by elemental analysis (EDAX) (Figure S3). Additionally, the cross-section of the TNF sheet was assessed using SEM. Figure 1 K confirmed that all the three nanofibrous layers were successfully preserved by the layer-by-layer approach and resulted in adequate adhesion with the adjacent layers
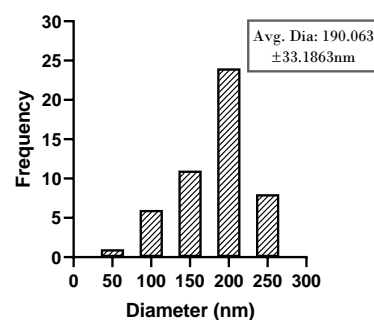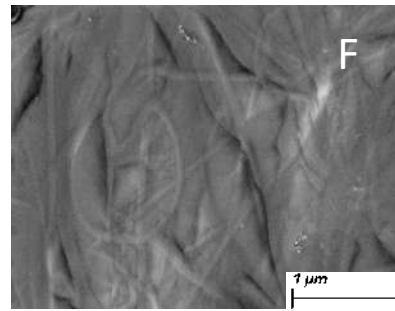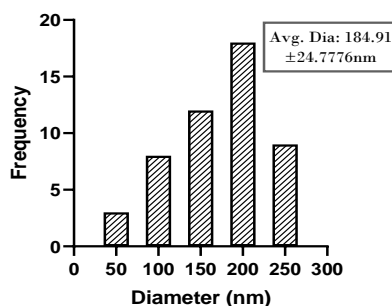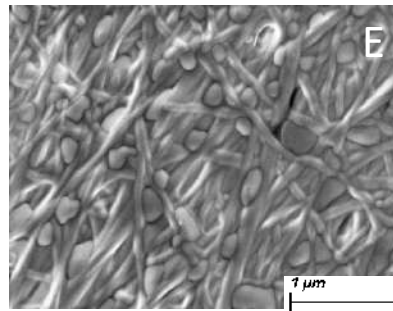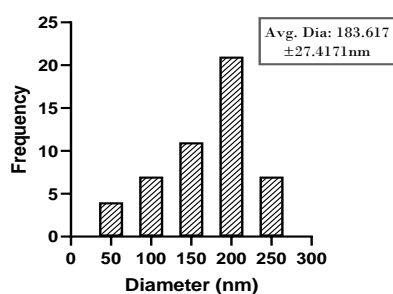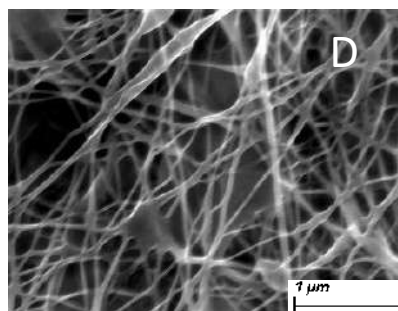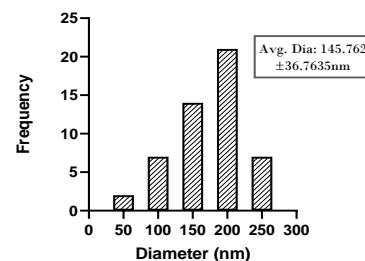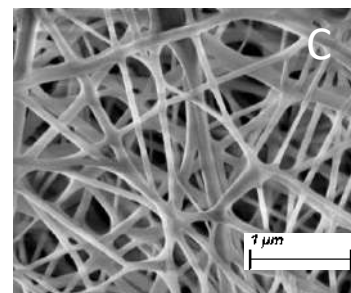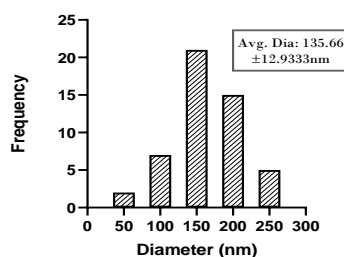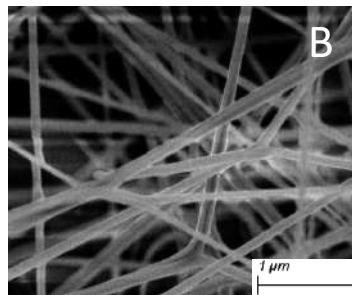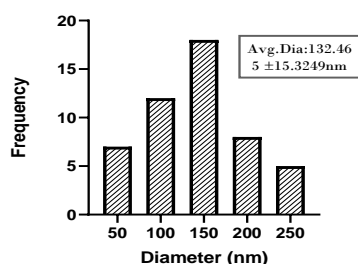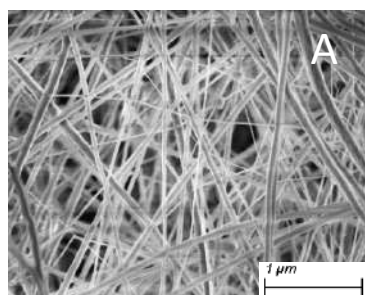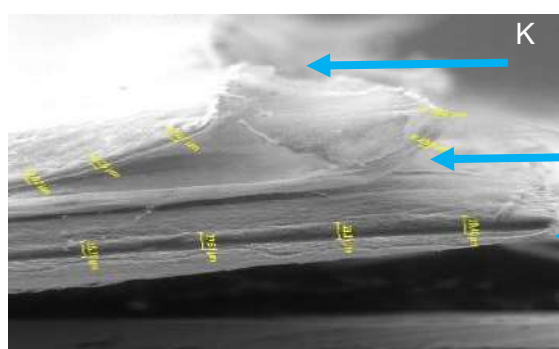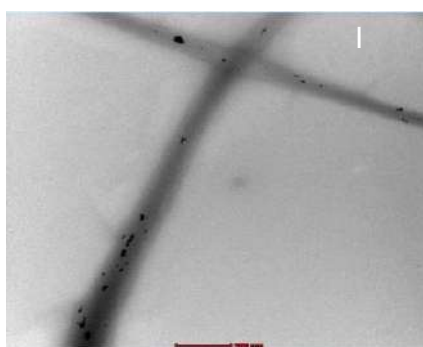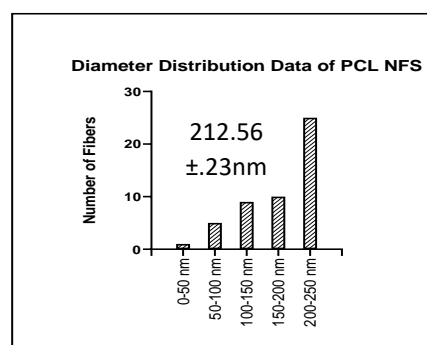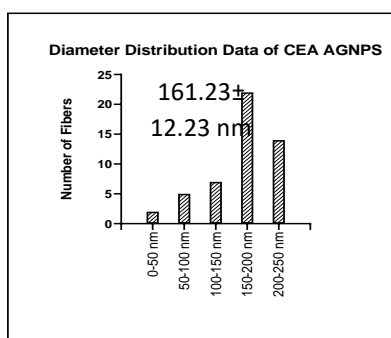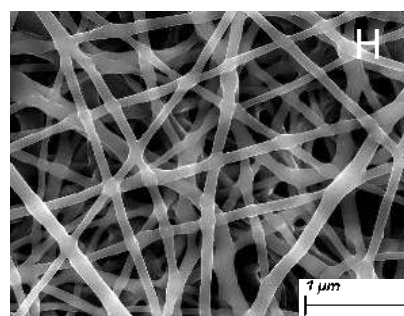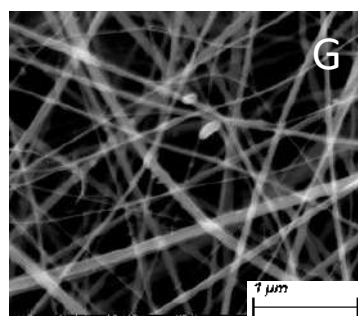
Figure 1 A) SEM image and diameter of the non-crosslinked PVA NF, B) crosslinked PVA NF (1%CA) C) cross-linked PVA NF (2%CA) D) crosslinked PVA NF (3%CA) E) cross-linked PVA NFs (4%CA) F) cross-linked PVA NFs (5%CA) G) AgNPs loaded CEA NFs H) the PCL NFs I-J) TEM image of AgNPs loaded in CEA NFs K) SEM image of the cross-section of TNF

5.3 Attenuated total reflectance infrared spectroscopy (ATR-FTIR)

Attenuated Total Reflectance Infrared Spectroscopy was used to investigate the functional groups in the manufactured mats, and to study any unfavourable interactions between the polymers during the electrospinning process. The spectra of PVA, CA, CEA and PCL were used as the controls and were compared with the spectra of the electropsun PVA NFs, cross-

linked PVA NFs, CEA NFs and PCL NFs. The FTIR spectra, as shown in Figure 2Aa, revealed the characteristic bands for PVA, exhibiting the presence of hydroxyl group (–OH) at $3297.60 cm^{-1}$, the -CH alkyl stretch at $2975.62 cm^{-1}$, the alcohol stretch at $1284.078 cm^{-1}$ and the C-O stretching at $1033.45 cm^{-1}$ [44] . The FTIR spectrum for the PVA NFs (Figure 2Ab) exhibited absorption bands at similar wavelengths, with slight shifts. The hydroxyl group resulted in a band at $3288.43 cm^{-1}$, the alkyl stretch was visible at $2983.33 cm^{-1}$, the alcohol stretch was seen at $1288.15 cm^{-1}$, while the C-O stretching was observed at $1048.32 cm^{-1}$, which confirmed the absence of any unwanted chemical interactions during the electrospinning process. The FTIR spectrum for CA (Figure 2Ac) exhibited a large and intense band at $3494.30 cm^{-1}$, which was attributed to the O-Stretching. The vibration bands observed at $3019.00 cm^{-1}$ and $2558.00 cm^{-1}$ corresponded to the C-H stretching. The peaks at $1753.19 cm^{-1}$ and $1721.83 cm^{-1}$ were assigned to the shift in the C=O vibration, due to the symmetric stretching of the COOH group of CA [45]. In case of the cross-linked PVA NFs (Figure 2Ad), all vibration bands of PVA were observed, in addition to the vibration band for C=O stretching of the COOH group of CA at $1733.00 cm^{-1}$ and $1715.09 cm^{-1}$, which confirmed that the PVA NF mats were successfully cross-linked with CA. The FTIR spectra of CEA (Figure 2Ae) and CEA NF (Figure 2Af) samples exhibited same bands, a smaller band at $2945 cm^{-1}$ due to the C-H stretching vibration in CA, the adsorption peak at $1730-1737 cm^{-1}$ due to the C=O stretching vibration of ester, the C-O and C-H bending vibrations at around 1228 and $1368 cm^{-1}$, respectively. The C-O stretching in CEA was seen as a wide band at $1050 cm^{-1}$ [46]. Similarly, the FT-IR spectra of PCL (Figure 2Ag) and PCL NF (Figure 2Ah) mats showed two characteristic peaks at $2943-2940 cm^{-1}$ and $2863-2855 cm^{-1}$, which corresponded to the stretching bands of the CH_2 groups. The absorption peak at $1730 cm^{-1}$ was ascribed to the stretching of the C=O groups, while the peaks at $1250-1300 cm^{-1}$ and $1150-1200 cm^{-1}$ belonged to the asymmetric and symmetric stretching of the C–O–C groups, respectively [47]. Thus, the FTIR spectra of the CEA NFs and the PCL NFs demonstrated the structural hallmarks as that of the pristine CEA and PCL, which suggested that there were no unwanted polymeric interactions that occurred during the electrospinning process.

5.4 Thermo-gravimetric analysis (TGA) of the nanofibrous mats

The thermal stability of the PVA, PVA NF, CA, PVA CA NF, CEA, CEA NF, NF, PCL and PCL NFs and TNF was assessed using TGA analysis. The degradation thermograms have been depicted in Figure 2B. The thermogram of PVA exhibited a three-stage degradation. The first loss of water molecules trapped in the hydrophilic PVA was observed at around 100 °C. The second loss occurred in the range of 200–380 °C, which was due to the loss of –OH groups and deacetylation of the PVA chains. The third degradation step was observed at 400–500 °C, which was attribute to the breakage of C-C and C-O bonds [48] . The thermogram of the PVA NFs showed a similar degradation profile as that of the pure PVA. The thermogram of CA revealed that the thermal decomposition of CA occurred in a single step, at 150-230°C [49]. However, the thermogram of the cross-linked PVA NFs indicated a better thermal stability as compared to the non-crosslinked PVA NFs, due to polymeric interactions between the free -OH groups of the PVA and the COOH groups of CA. As shown in Figure 2B, the thermogram of pure CEA showed three degradation steps. The first loss from the hydrophobic CEA was observed at around 100 °C, which was attributed to the presence of moisture. The second

intensive peak at 250–350 °C was observed due to the loss of –COO groups and deacetylation of CEA. The third degradation step was observed at 350–450 °C, which was attributed to the breakage of C-C and C-O bonds [50]. However, the thermal decomposition profile of the CEA NFs exhibited better thermal stability as compared to the native CEA. The gravimetric analysis of PCL, PCL NFs, showed two stage degradation, as depicted in Figure 2B. The first loss was observed in the range of 200–300°C, due to the loss of C=O groups, while the second degradation step observed at 400–500 °C was attribute to the breakage of C-C and C-O bonds [51]. Thus, the spectra revealed that the PCL layer had greater thermal stability. The thermogram of TNF demonstrated slower thermal deposition and greater thermal stability, as compared to single polymeric sheets, which was attributed to the interaction between the polymers constituting the different layers during electrospinning, which led to polymer chain elongation.

5.5 X-ray crystallographic analysis

The crystalline or amorphous nature of PVA, PVA NF, CA, PVA CA NF, CEA, CEA NF, PCL and PCL NF were successfully studied using powder XRD, as shown in Figure 4. The XRD of pure PVA (Figure 2Ca) exhibited characteristics of crystalline and amorphous phases of conventional semi-crystalline polymers. It showed several distinct crystalline peaks at $2\theta = 11.211°, 19.450°, 20.654°, 23.520°$ [52]. These peaks were not observed in the PVA NF (Figure 2Cb), which indicated that the crystalline state of PVA was converted into an amorphous one after electrospinning. The X-ray diffraction pattern of pure CA (Figure 2Cc) exhibited peaks at $2\theta=14°, 19°, 26°$, with high intensity [53]. However, no characteristic peaks were observed for CA at 2θ 14°, 19°, 26° in the cross-linked mats (Figure 2Cd). The X-ray diffraction pattern of CEA exhibited peaks at $2\theta = 14°, 20°$ and 25°, with slight intensity, as depicted in Figure 2Ce[54]. However, no characteristic peaks were observed for CEA NF (Figure 4f). Figure 4g depicts the XRD patterns of PCL, with three significant diffraction peaks at $2\theta=21.3°, 27°$ and 29° [55], which were also observed in PCL NF (Figure 2Ch). Thus, the XRD pattern of PVA, PVA NF, CEA and CEA NFs revealed that during the electrospinning process, the semi-crystalline and crystalline polymers were converted into the amorphous form, possibly due to polymer chain entanglement or polymer chain scission during electrospinning. However, the PCL NFs were able to withstand their crystalline structure even after electrospinning, which allowed for controlled release of AgNPs Finally, the semi crystalline nature of the TNF mat was depicted by the diffraction pattern observed at $2\theta = 29°$ (Figure 2Ci).
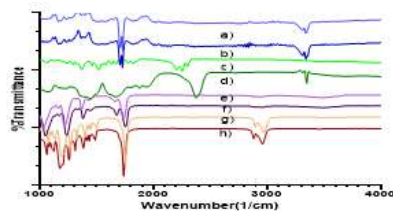
Figure 2A) Overlay of FTIR spectra of PVA, PVA NF, CA and PVA CA NFCEA, CEA NF, PCL and PCL NF
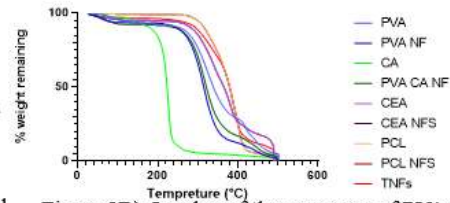
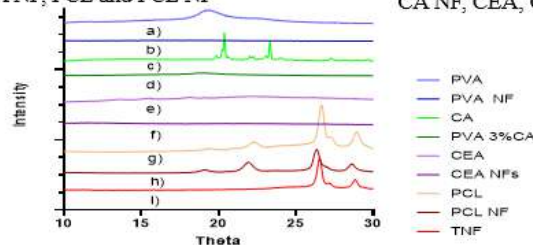Figure 2B) Overlay of thermograms of PVA, PVA NF, CA, PVA CA NF, CEA, CEA NF, PCL, PCL NF and TNF

Figure 2C) Overlay of diffractograms of PVA, PVA NF, CA, PVA CA NF, CEA, CEA NF, PCL, PCL NF and TNF

5.6 Water uptake by the nanofibers

The NFs' capacity to absorb water is essential for controlling nutrient delivery, infiltration, and cell adhesion. In the present study, the water absorption capacity of the PVA CA NF, CEA NF, CEA AgNPs NF, PCL and TNF mats were evaluated over 14 days. Figure 3 shows the percentage of water uptake for fabricated nanofiber mats. The samples were weighed at specific time intervals and the percent weight gain was calculated. In case of all the NF mats, the water retention properties increased till 7 days. After 7 days, there was no significant increase in water retention by all the mats. This may have been due to the bonding between the free COOH groups of the cross-linked PVA with the OH groups of water. Since after 7 days there was saturation of the available COOH groups for interaction with the OH groups of water, there was a decrease in the water retention properties of the mats after a week [56]. Also, CEA NF without AgNPs exhibited greater water retention as compared to the CEA NF loaded with AgNPs. This was attributed to the bonding of AgNPs with the nano porous structure of the NF mats [57]. Also, PCL exhibited lower water retention as compared to the CEA NF due to its superhydrophobic nature. However, the combination of these layers in the TNF sheets, loaded with AgNPs, resulted in water uptake capability of upto 200%, till 15days. There is no significant difference in the uptake study in comparison of PVA NF, CEA NF , CEA AgNPs, PCL NFs with respect to TNF AgNPs (P>0.05). However, values obtained indicated that the fabricated sheet having significant water uptake study sufficient for wound healing applications [58].
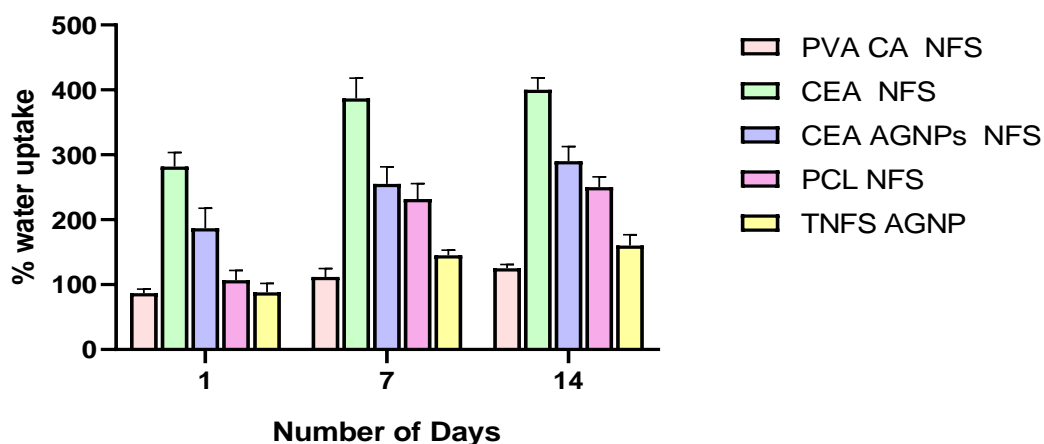
694

695   Figure 3 Graphical Representation for water uptake study of PVA CA NF, CEA NF, CEA

696   AgNPs NF,PCL NF and TNF

697

5.7 Water vapour transmission rate

699   Reduction in the risk of and faster healing are largely dependent on the permeability of the
700   wound dressings to absorb oxygen and wound exudates. The optimum dressing should be
701   permeable enough to prevent excessive evaporation and collection of wound exudates, as this
702   could cause the wound site to dry out and cause pain when the dressing is changed. [59]. The
703   WVTR can be used to assess a dressing's capacity to reduce water loss. By using different
704   wound dressings with varied WVTRs, the wound surface moisture can be controlled. Previous
705   research indicates that the evaporation rate in healthy skin ranges from 204 to 250 g/(m2 ·day),
706   but depending of the type of damage, it can reach 5000 g/(m2 ·day).According to research, the
707   optimal weight-to-rapidity ratio (WVTR) for wound dressings to provide proper moisture
708   retention at the wound site and avoid secretion accumulation is between 2000 and 2500 g/(m2
709   ·day) [60, 61] In the present investigation, the WVTR of the NF mats was evaluated using the
710   water cup method, as reported in the literature, with slight modifications. The loss of weight of
711   water was calculated at an interval of 24 h and transmission rate was evaluated. The values for
712   WVTR for PVA CA NF, CEA NF, CEA AgNPs NF, PCL and TNF have been stated in Table
713   1.We concluded that the TNF sheet dressing with a WVTR of approximately
714    $192.50\pm3.189g/m^2$ /24 h g/m^2 /24 h could maintain the optimal moisture content required for
715   cellular proliferation and functioning of human keratinocyte cells.

716

5.8 Porosity of nanofibrous sheets

718   The films' porosity, an essential structural component for biomedical applications, was
719   assessed in the study. By examining the material's porosity, the nanofibrous dressing's
720   absorption capacity was calculated., The porosity of dressings between 60 and 90% permits
721   oxygen permeability, cellular adhesion, migration, and proliferation for skin regeneration.
722   It also inhibits bacterial infiltration[62]. On the other hand, wound dressings with a porosity
723   of less than 60% may prevent gas permeability, vascularization, cellular ingrowth, and
724   nutrient diffusion, while those with a porosity of more than 100% may find it more difficult
725   for cells to occupy the voids in the structure. [62] . In the present study, porosity of PVA
726   CA NF, CEA NF, CEA AgNPs NF, PCL and TNF were investigated using liquid

727 displacement method. The porosity of AgNPs has been has been increases due to reduction
728 in water uptake of CEA nanofibers in presence of AgNPs which can have a significant
729 effect on the results of wettability, biocompatibility, and cell growth [57, 63]. The porosity
730 values of PVA CA NF, CEA NF, CEA AgNPs NF, PCL and TNF have been stated in Table
731 1, which revealed that the fabricated NF mats had appropriate porosity for wound healing
732 properties.

733 Table 1 Water vapour evaporation rate and % porosity of PVA CA NF, CEA NF, CEA
734 AgNPs NF, PCL NF, TNF

Sample Name	Water vapour transmission rate (g/m2 /24 h)	% Porosity
PVA CA NF	192.70±1.020	90.52±2.42
CEA NF	192.30±4.55	87.01±1.36
CEA AgNPS NFs	191.2 ±1.523	88.86±2.72
PCL	200.8°± 3.800	93.6±1.70
TNF	192.50±3.189	85.75±1.80

735
736 **5.9 Contact angle measurement**
737 The hydrophilic and hydrophobic properties of the NF mats was successfully measured and has
738 been shown in Figure S4. The contact angle for PVA NF, CEA NF and PCL layer were found
739 to be 36.88°, 65.59°, and 106.9.0°. Thus, the top layer of the TNF mat was hydrophilic due to
740 the presence of PVA, the middle layer was hydrophobic because of the presence of CEA, while
741 the bottom layer was super hydrophobic because of the presence of PCL. The contact angle of
742 the TNF was found to be 55.66°. Since, the inner layer of PCL shows hydrophobic behaviour,
743 it would play an imperative role in significant adhesion of cells and protect the mats from getting
744 wet, rendering the TNF mat suitable for wound healing applications.
745
746 **5.10 *In vitro* degradation studies**
747 The presence of enzymes in biological fluid cause the NFs to begin deteriorating as soon as it
748 comes into touch with bodily fluids. Therefore, prior to doing an in vivo investigation, it is
749 imperative to examine the material's *in vitro* deterioration. Examining the rate of degradation
750 and the amount of time needed for the produced NF mats to degrade, as well as whether the
751 mats could last the 15 days needed for natural skin regeneration, was the primary goal of the *in*
752 *vitro* degradation analysis. The degradation of mats was studied in a medium containing the
753 enzyme that is present at the wound sites. The medium was chosen to mimic the natural
754 environment (pH) of the body fluids. The mats were incubated at 37 °C in phosphate buffer
755 saline having a pH of 7.4, which contained chicken lysozyme (10000 U/mL in PBS). The
756 degradation was analysed on days 1, 7, and 14 by measuring the loss of their initial mass of the

NF mats. Figure 4 depicts the degradation percentage of the PVA CA NF, CEA NF, CEA AgNPs NF, PCL NF, TNF. The PVA CA NF demonstrated faster degradation rate, as compared to the CEA and PCL NF mats, due to the hydrophilic nature of the PVA. Fascinatingly, due to cross-linking of the PVA NF, they were able to maintain its stability till 15 days. The PCL NF exhibited slower degradation rate as compared with the other NF mats due to its superhydrophobic nature. While the CEA NF mat exhibited a moderate degradation rate. The degradation rate for AgNPs loaded NF mat was lower than that of the CEA NF alone. This was due to the fact that the addition of nanoparticles produced intermolecular polymeric connections that shielded the polymer incision sites from the fluid seeping through the mats. As the nanocomposites increased, they acted as a diffusion barrier that hindered the swelling and prevented the degradation of NF mats [54]. The TNF showed faster degradation initially due to the direct interaction between the hydrophilic PVA layer with the medium. However, the presence of hydrophobic polymers in the TNF mat was able to prevent its rapid degradation. Unlike water uptake study is no significant difference in the degradation profile of PVA NF, CEA NF , CEA AgNPs, PCL NFs in comparisons with TNF AgNPs ($P > 0.05$) Thus, there was a strong correlation between the water uptake investigation and the *in vitro* degradation study. It was also expected that the material's breakdown would facilitate the creation of fresh extracellular matrix (ECM) at the site of the wound, by creating space for tissue growth and differentiation.
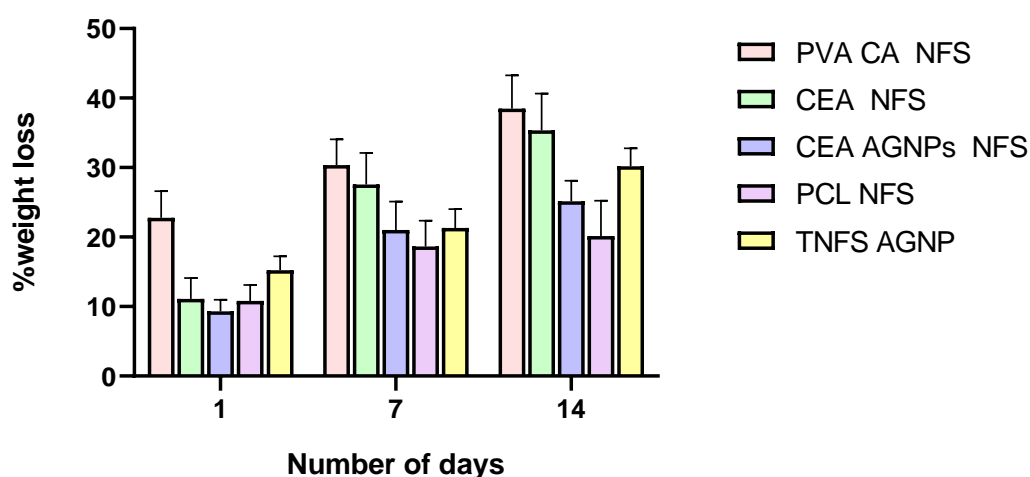

Figure 4 Graphical Representation for *In vitro* degradation study study of PVA CA NF, CEA NF, CEA AgNPs NF, PCL NF and TNF

5.11 Mechanical strength analysis
Until the wound heals, the wound dressing must shield it from all types of external stress. Furthermore, especially when treating wounds close to joints, the wound dressing needs to be flexible enough to move with the body while staying in place. To encourage the best possible healing of the injured tissues, it is essential to choose a dressing with the appropriate mechanical properties. The mechanical strength of the PVA NF, PVA CA NF, CEA NF, CEA AgNPs NF, PCL NF and TNF were studied using a electroforce 5500 model (TA, instruments USA). Several studies have reported varying values of tensile strengths, ranging from 0.7 to

789 18.0 MPa, as being sufficient for dermal cell culture [64, 65]. The mechanical strength of PVA,
790 PVA CA NF, CEA NF, CEA AgNPs NF, PCL NF and TNF were observed as 2.88 ±0.25M.
791 Pa, 6.82 ±0.37 M. Pa, 1.22 ±0.0. 35M.Pa, 1.55, 1.55 ±0.45M.Pa , 11.90±0.77 M. Pa and
792 12.70±0.606 MPa, respectively. The mechanical strength for outer PVA CA NF and middle
793 CEA AgNPs showed significant difference (P<0.05). Also the mechanical strength of middle
794 CEA AgNPs in comparison with TNF containing PCL layer showed significant difference
795 (P<0.05) which confirmed that PCL impart high mechanical strength to TNF due to its super-
796 hydrophobic nature which is required for tissue engineering application . Asghar Eskandarian
797 et al investigated for mechanical strength there developed single layered propolis embedded
798 polyurethane-hyaluronic acid (The PU-HA/1% EEP) nanofibrous wound dressing and
799 bilayered wound dressing composed of a dense polyurethane/propolis membrane and a
800 biodegradable polycaprolactone/gelatin nanofibrous Scaffold (PU/EEP-PCL/Gel) which was
801 found as 4.86 ± 0.9MPa and 5.6 ± 0.6 MPa respectively [66, 67]. Thus in comparison with this
802 we confirmed that the fabricated nanofiber dressing was suitable for wound dressing and skin
803 tissue regeneration.

804 **5.12 Evaluation of cellular toxicity using MTT assay**
805 The *in-vitro* cytotoxicity of PVA NFs, PVA CA NFs CEA NFS, AgNPs loaded CEA NFs, PCL
806 NFs and TNF were assessed using MTT assay. Human fibroblast cells and keratinocytes cells
807 were used for these studies. Human fibroblast cells are present in dermal layer of skin, which
808 play an imperative role in secretion of collagen and other proteins that maintain the
809 extracellular structure of the skin. While the keratinocytes are present in the epidermal layer of
810 the skin and prevent the skin from environmental damage due to heat, pathogenic bacteria.
811 Thus, an ideal wound dressing should be biocompatible with these skin cells. The cytotoxicity
812 of the fabricated mats have been depicted in Figure 5A and 5B. The cell viability with PVA
813 NFs, PVA CA NFs CEA NFS, AgNPs loaded CEA NFs, PCL NF sand TNF were observed as
814 97.75112 ±2.33 % , 97.77661± 2.8% , 94.4028± 1.48%, 98.90055 ±1.07% , 93.45327± 2.6%,
815 99.17± 1.6%, respectively, in case of the HDF cells. While in case of the HeCat cell, these
816 values were $80.47337 \pm 1.01\%$, $72.51 \pm 1 2.16\%$, $78.6 \pm 4.2\%$, $91.6 \pm 1.95\%$, $79.0 \pm 1.52 \%$,
817 $76.9 \pm 5.23\%$, respectively, for PVA NFs, PVA CA NFs CEA NFS, AgNPs loaded CEA NFs,
818 PCL NF sand TNF. As per ISO 10993-5[68], if a material shows cell viability of greater than
819 70%, it is considered as non-toxic for medical application. Thus, the MTT data indicated that
820 the fabricated nanofiber dressings were safe for application over the wound sites.
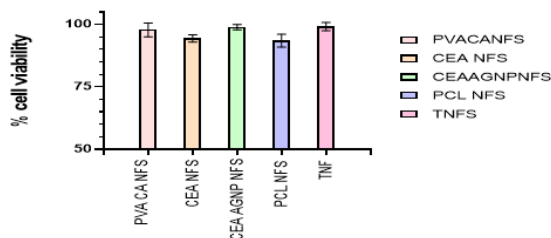

Figure 5A Graphical Representation for cellular cytotoxicity studies for PVA NF, PVA CA NF, CEA NF, CEA AgNPs NF, PCL NF and TNF against HDF cells
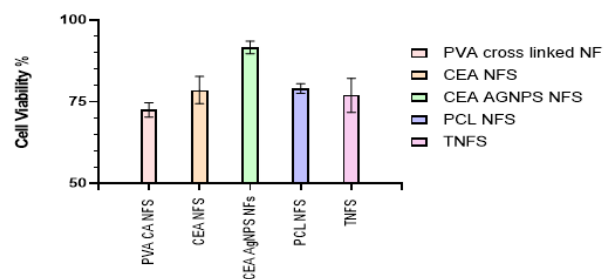
Figure 5B Graphical Representation for cellular cytotoxicity studies for PVA NF, PVA CA NF, CEA NF, CEA AgNPs NF, PCL NF and TNF against HecaT cells

821
822

5.13 Cellular proliferation study using EZ blue assay

The cellular proliferation with PVA NFs, PVA CA NFs CEA NFS, AgNPs loaded CEA NFs, PCL NFs and TNF were assessed using EZ Blue assay and HaCaT and HDF cells, considering the end-application of NF mats in wound healing. The growth of HaCaT and HDF cells was studied on days 1, 2 and 3. In the EZ Blue™ cell assay, the mats were observed to serve as good templates for cell proliferation. The percentage of cell proliferation was calculated by comparing the proliferation of the cells recorded at 24 hours with that observed at 48 and 72 hours., as depicted in Figure 6A and 6B. The proliferation data showed that all the samples showed significant increase in cell viability after 48 h, upto 150 %, in case of both the cell types. The cell proliferation for PCL layer was found to be maximum in comparison with the cross-linked PVA layer and CEA NF, possibly due to the superhydrophobic nature of PCL, which may have allowed the cells to adhere well and support their growth. The cell proliferation in case of TNF was comparable to the that of PCL, as PCL layer was used as the bottom layer in the TNF mat for its significant adhesion and painless removal. Thus, this investigation confirmed that the fabricated NF mats were appropriate for cell growth and proliferation and henceforth rapid wound healing [69].
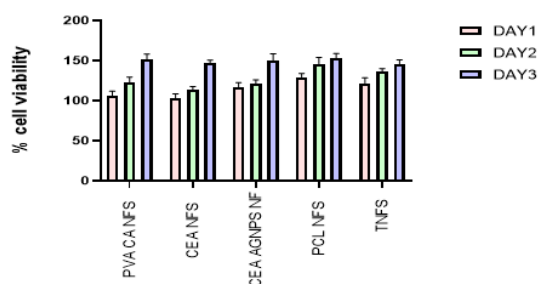

Figure 6A Graphical Representation for cellular proliferation studies for PVA CA NF, CEA NF, CEA AgNPs NF, PCL NF and TNF against HDF cells
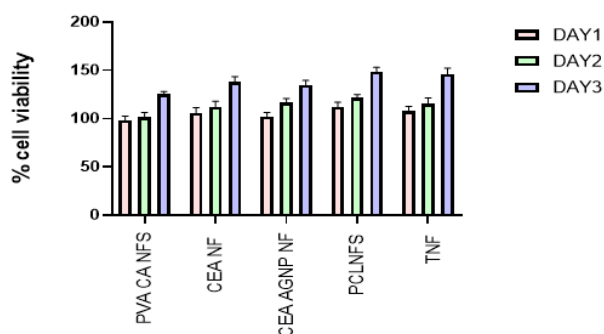
Figure 6B Graphical Representation for cellular proliferation studies for PVA CA NF, CEA NF, CEA AgNPs NF, PCL NF and TNF against HacaT cells

5.14 Thrombin generation assay to assess the haemostatic activity

A sensitive and precise marker used to analyse the thrombin production in blood over time is the thrombin-antithrombin (TAT) complex. The ELISA (Enzyme Linked Immunosorbent Assay) kit for thrombin-antithrombin complex (TAT) human in vitro is intended for the quantitative evaluation of thrombin-antithrombin complex quantities in plasma. Here, a specific antibody is pre-coated onto the 96-well plates and blocked. In this investigation, the quantification of the thrombin-antithrombin complex was carried out to provide information about the coagulation process with the NF mats. The dressing material comes into direct contact with the wound and stops the blood flow via coagulation of blood at the wound sites. In order to ascertain how the developed dressing material will react to the coagulation process, the TAT test was carried out. Over the course of one hour, the amount of thrombin produced by the plasma incubated with the dressing material was measured in ng/mL and compared to the standard, namely gauze. The TAT analysis results are shown in Figure 7, which shows that the electrospun mats effectively generated thrombin in comparison to the untreated and gauze-treated blood samples. Accordingly, the study suggested that the presence of polymeric NF mats

may enhance thrombin synthesis and cause blood clotting, which would then promote successful wound healing [70].
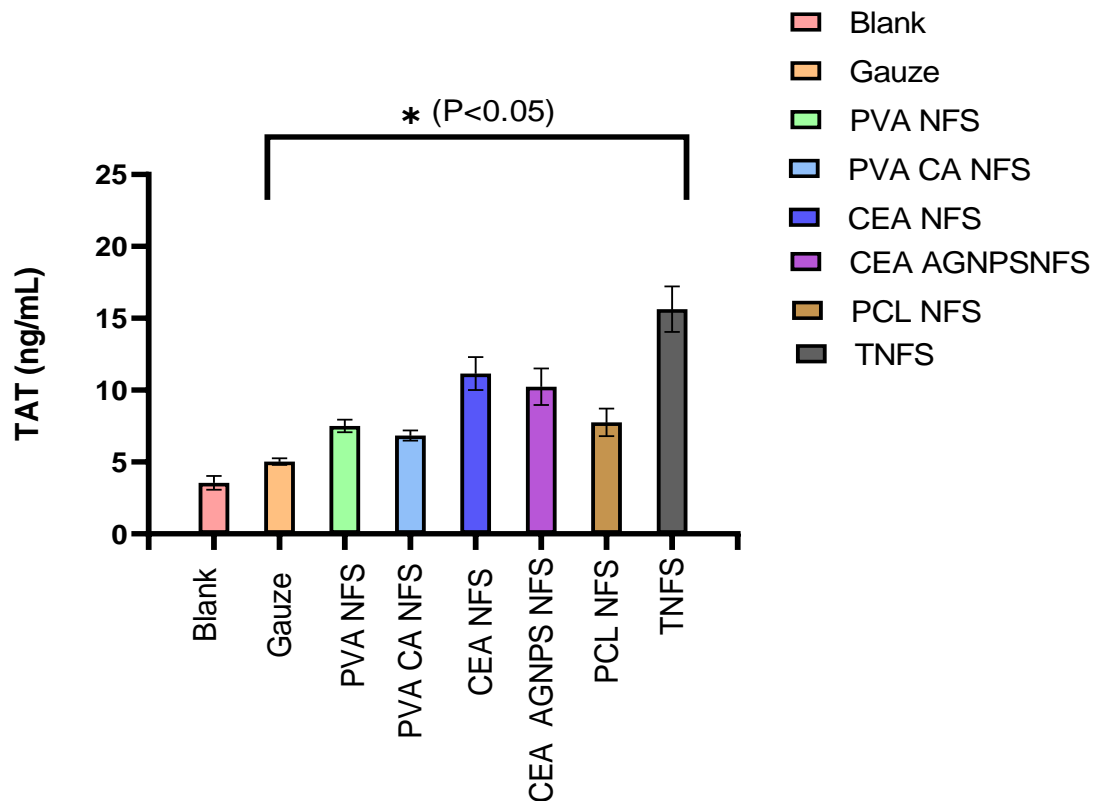

Figure 7 Graphical Representation for thrombin generation using TAT assay for PVA, PVA NF, PVA CA NF, CEA NF, CEA AgNPs NF, PCL NF and TNF in comparison with gauze *(*) represented a p value of < 0.05, indicating its significant difference as compared to the controls.*

5.15 Loading and release characteristics of AgNPs

Before examining the silver release properties from the TNF mat containing AgNPs, the amount of silver loaded in the mats was calculated, and for the TNF mat made with 200 ppm of the AgNPs, the result was 0.524 mg/mL mg/g considered as 99.89 ± 1.10 percent of the initial AgNPs content added to the electrospinning solution was accounted for by this. The release characteristics of Ag+ ions from TNF containing AgNPs was investigated by total immersion method, in PBS (pH7.4) containing lysozyme (10,000 U/mL). The *in vitro* AgNPs release profile from the NF mat was observed as shown in Figure 8. The profile exhibited an initial burst release, followed by a controlled release of AgNPs from the CEA NF in PBS, over time. Over the first 8 h, 30-40% of AgNPs were released, followed by a controlled release of upto 65% till 7 days. Thus, controlled release of AgNPs from TNF may prevent the wound from bacterial infection and hence support in wound healing. As indicated in Table 2, the release parameters, namely n—release exponents—release rate constant; and r^2—regression coefficient, were primarily considered in order to comprehend the mechanism of AgNPs. The best fit model was chosen based on goodness of fit, and it explained the anomalous release by releasing, diffusing, and eroding the polymeric matrix in that order [71].
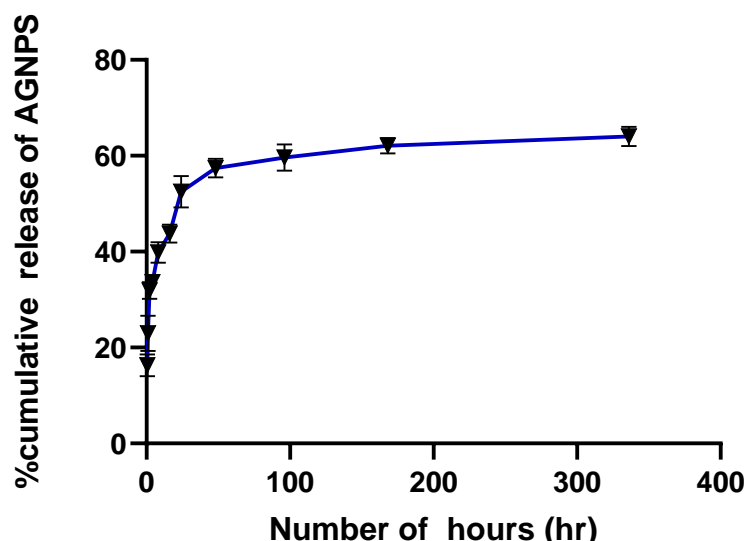
Figure 8 Graphical representation for release of AgNPs through TNF

Table 2 *In vitro* drug release kinetic models and regression output for AgNPs release from TNF

Sample	Dissolution Medium	Percent Drug Released* (24 h)	Release Exponent (n)	Drug Transport Mechanism	Release Constant (k)	Regression (r²)	Best Fit release Model
AgNPs in TNF	PBS (7.4)	52.47	0.6717	Anomalous Transport	12.1644	0.850	Hix. Crow

5.16 Antibacterial evaluation

Using the disc diffusion method, the bactericidal activity of TNF loaded with AgNPs (200 ppm) was evaluated. The activity was conducted against common wound-associated microbes namely *Escherichia coli* (*E. coli*) and *Staphylococcus aureus* (*S. aureus*). As a control, the activity of AgNPs suspension at a comparable concentration was employed. After analysis, it was discovered that the diameters of the zones of inhibition, which indicate the death of the organisms, were 2.5 ± 0.23 for AgNPs and 1.98 ± 0.12 for TNF against E. coli, and 2.06 ± 0.16 for AgNPs and 1.76 ± 0.09 for TNF against S. aureus, respectively. Three studies were conducted in duplicate. The antibacterial activity of single layered a propolis embedded polyurethane-hyaluronic acid (PU-HA/1% EEP) and bilayer wound dressing composed of a dense polyurethane/propolis membrane and a biodegradable polycaprolactone/gelatin nanofibrous Scaffold (PU/EEP-PCL/Gel) investigated using disc diffusion method which showed zone of inhibition against *Staphylococcal aureus* (5.4 ± 0.3 mm, 2.36 ± 0.33), *Escherichia coli* (1.9 ± 0.4 mm, 3.18 ± 0.63) for PU/EEP-PCL/Gel and PU-HA/1% EEP respectively which is quite comparable with proposed dressing [66, 67]. The AgNPs acts through following mechanism, formerly AgNPs releases slowly from polymeric matrix of triple layered dressing. Further, due to electrostatic interaction between positively charged

AgNPs and negatively charged bacterial cell wall membrane, AgNPs remains adhered to the membrane surface of microbial cells, by modifying the lipid bilayer and increasing the membrane permeability, followed by intracellular penetration of AgNPs. Then Silver nanoparticle oxidized into aqueous environment of cytoplasm in presence of oxygen and lead to generate the reactive oxygen species and free radicals which are responsible to damage the intracellular micro-organelles like mitochondria, ribosomes, and vacuoles and biomolecules including DNA, protein, and lipids and cause the cell death [72]. There is difference in antibacterial activity of AgNPs against gram positive and gram negative bacterial due slight changes in structural hallmarks of their bacterial cell wall Gram-negative bacteria's outer cell membranes are mostly composed of lipopolysaccharide (LPS) and L-a-phosphatidyl-ethanolamine (PE), two amphiphilic macromolecules that are found in lesser amounts in gram-positive bacteria. Since LPS and PE prevent AgNPs from interacting with cell membranes, these AgNPs were less effective against gram-negative bacteria than gram-positive bacteria.[73]

5.17 Wound area measurement

The effectiveness of artificially generated AgNP-loaded TNF nanofibrous mats for wound healing was assessed by contrasting them with commercially available cotton gauze, a conventional dressing. The rats with open wounds were considered the negative control group, and the rats treated with cotton gauze were considered the positive control group. The wound areas on days 0, 3,7,10 was measured for all the groups and the rate of wound healing was calculated as shown in Figure 9. On day three, the rate of wound healing with AgNPs loaded TNF dressing was 64.19%, compared to 53.18% and 10.54 % for the positive control group and negative control groups, respectively. On day 7, the positive control group (60.94%) and the negative control (28.55%) had worse wound healing rates than the AgNPs loaded TNF nanofibrous dressing (80.28%). Day 10: The group with AgNPs loaded TNF nanofibrous dressing had the highest wound healing rate of all the groups, at 90.28%. In Figure 13, the wound healing rate was greater in the AgNPs loaded TNF dressing group than in the negative control group (p, 0.0160 < 0.005). As a result, TNF nanofibrous dressing covered with AgNPs showed promise for usage as a wound dressing in contrast to cotton gauze, a conventionally marketed treatment. The dressing's high surface area-to-volume ratio and nanofibrous composition, which may have led to increased absorption of the wound exudates, were credited with promoting this better healing. Moreover, the hydrophilic polymer of the uppermost PVA CA NF layer more effectively absorbed the wound exudates. While the PCL layer's porous structure may have preserved optimal cellular respiration and water and gas permeability, preserving a moist environment at the wound site, the CEA layer containing AgNPs demonstrated a better degree of therapeutic efficacy. Consequently, when taken as a whole, the multipurpose nature of every TNF dressing layer. Thus collectively, the multifunctionality of each layer of the TNF dressing may have resulted in more effective wound healing as compared to the traditional gauze. Asghar Eskandarian et al investigated *invivo*-efficacy of single layered a propolis embedded polyurethane-hyaluronic acid (The PU-HA/1% EEP) nanofibrous wound dressing using wistar rats' skin wound model. Th full thickness model was created and monitored for 21 days. After 21 days wound treated with the PU-HA/1% EEP showed higher closure of wound area upto 97%. Fascinatingly, wound specimen histologically examined on the 21st day with PU-HA/1% EEP showed well-developed dermis according to the presence of hair follicles and lower number of inflammatory cells in comparison with other groups. Furthermore, the PU-HA/1% EEP showed more densely packed collagen fibres with a parallel arrangement in the extracellular matrix in comparison with other groups confirmed by

Masson's trichrome. Additionally, Asghar Eskandarian et al also investigated *in-vivo* efficacy of bilayer wound dressing composed of a dense polyurethane/propolis membrane and a biodegradable polycaprolactone/gelatin nanofibrous Scaffold (PU/EEP-PCL/Gel) using the efficacy of the wound Wistar rats' skin wound model. Full-thickness defects (11 mm × 11 mm) were created on the back of the mice and monitored for 15 days. On 15th days the bilayered PU/EEP-PCL/Gel wound dressing treated group exhibited approximately 100% healed and closed wounds at this day. Additionally, the Haematoxylin and eosin staining of bilayered PU/EEP-PCL/Gel group specimens exhibited significantly more developed dermis in comparison with control specimens due to presence of lower number of inflammatory cells and development of more hair follicles while the specimens were stained with Masson's trichrome also confirmed for more   Collagen deposition at the wound matrix plays a critical role in the healing process, as it provides scaffolds for wound-healing cells [66, 67].
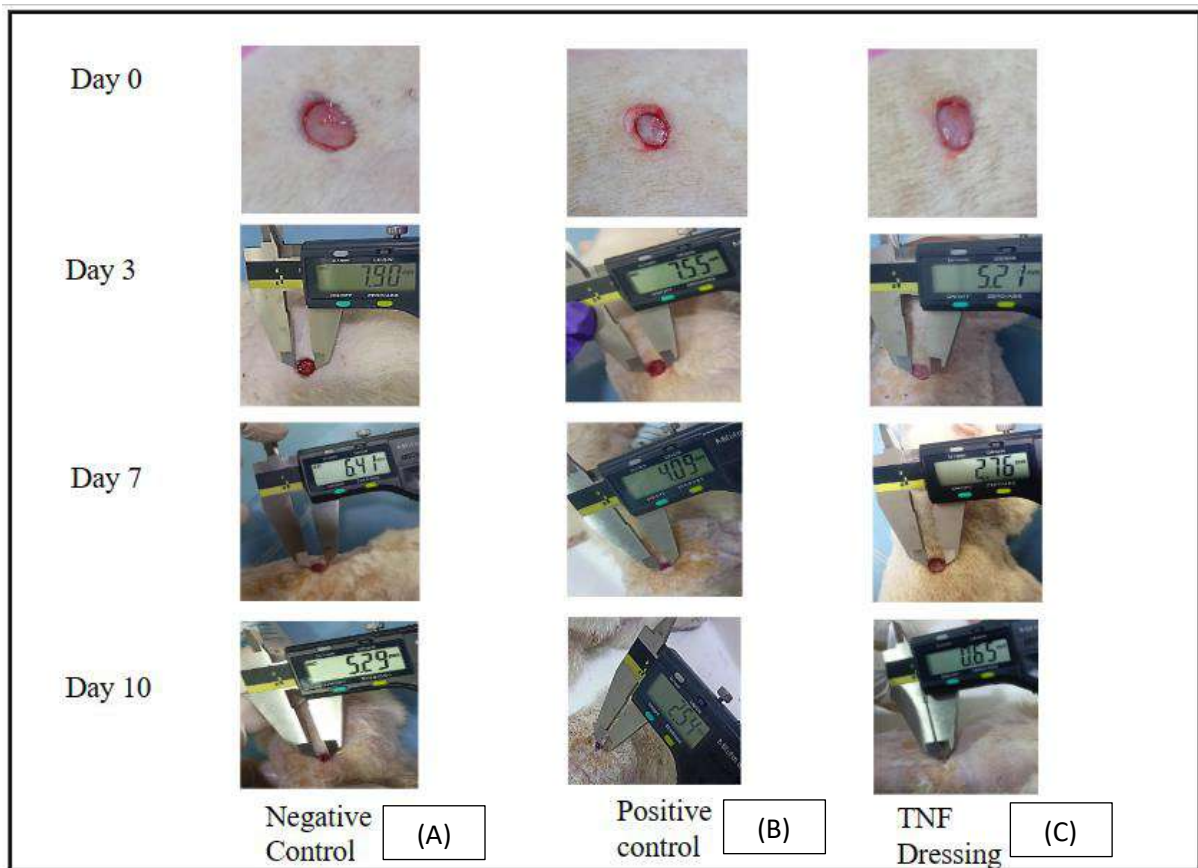

Figure 9 Photographs of an in vivo wound healing study. A group is negative control , B group is positive control and C TNF with AgNPs.
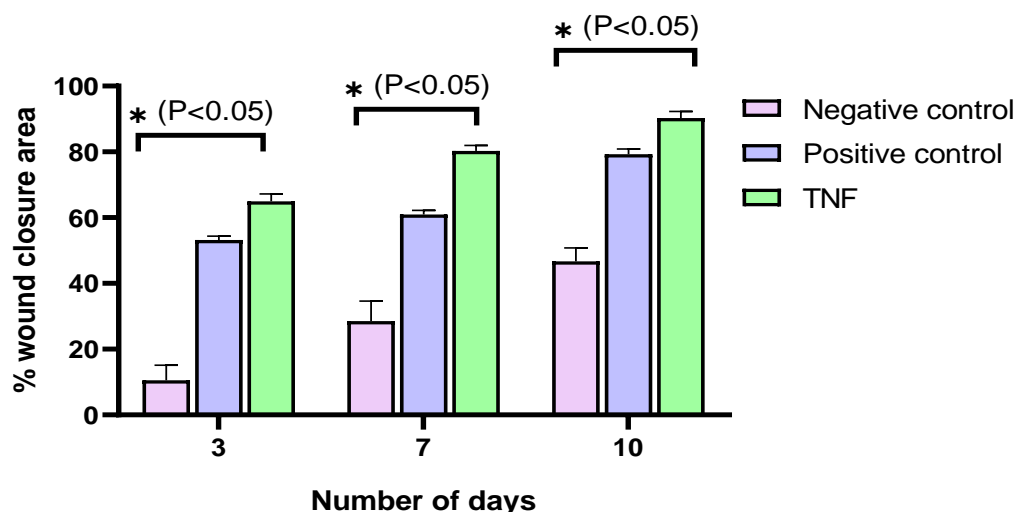
Figure 10Comparison of wound healing rate of TNF with AgNPs with positive control (cotton gauze) and negative control (open wound). Wound healing rate *(*) represented a p value of < 0.05, indicating its significant difference as compared to the controls.*

5.18 Haematoxylin and eosin/ Masson's trichrome staining

Haematoxylin, a complex form of aluminium ions, and oxidized haematoxylin, which imparts blue color to the cellular nuclei and keratohyalin granules, are used in the Haematoxylin and Eosin (H & E) staining procedure. After nuclear staining, eosin is used as a counterstain, giving the eosinophilic and other structures pink and red hues. In order to stop the tissue from degrading, three samples of rat skin one from an open wound, one treated with AgNPs-loaded TNF, and one cotton gauze dressing were sliced into five-by-five centimetres and put in a 10% formalin solution. After the tissue was embedded in paraffin blocks, paraffin slices were produced on slides for H&E staining. After then, these slides were examined under a microscope. The histological pictures of the injured tissue at day 10 are displayed in Figure 14 for the following three groups: A) negative control (open wound), B) positive control (cotton gauze group), and C) AgNPs loaded TNF. Histological studies demonstrated that in the case of the negative control group Figure 11 A, there was mild re-epithelization of the stratified squamous epithelium maturation with less formation of the keratinised layer. There was presence of a few fibroblast cells along with multifocal area of proliferation, focal area of re-epithelization, multifocal area of angiogenesis, focal area of proliferation fibroblast, which suggested that the wound was in proliferation stage. Figure 11B shows moderate reepithelization of the stratified squamous epithelium with multifocal area of the stratified squamous epithelium maturation, with complete proliferation of fibroblasts and multifocal area of angiogenesis, along with slight formation of thin and thick bundle of collagens. While figure 11 C showed complete re-epithelization of stratified squamous epithelium along with complete maturation of collagen fibres, multi-focal area of angiogenesis with complete proliferation of fibroblasts. Furthermore, the development of an unbroken keratinized layer in the epidermis indicated that the wound healing maturation stage had complete. [74]. Thus, the study concluded that AgNPs loaded TNF exhibited the fastest and the most efficient wound-healing, much superior to the traditional dressing material, via a natural healing mechanism (Figure 11).
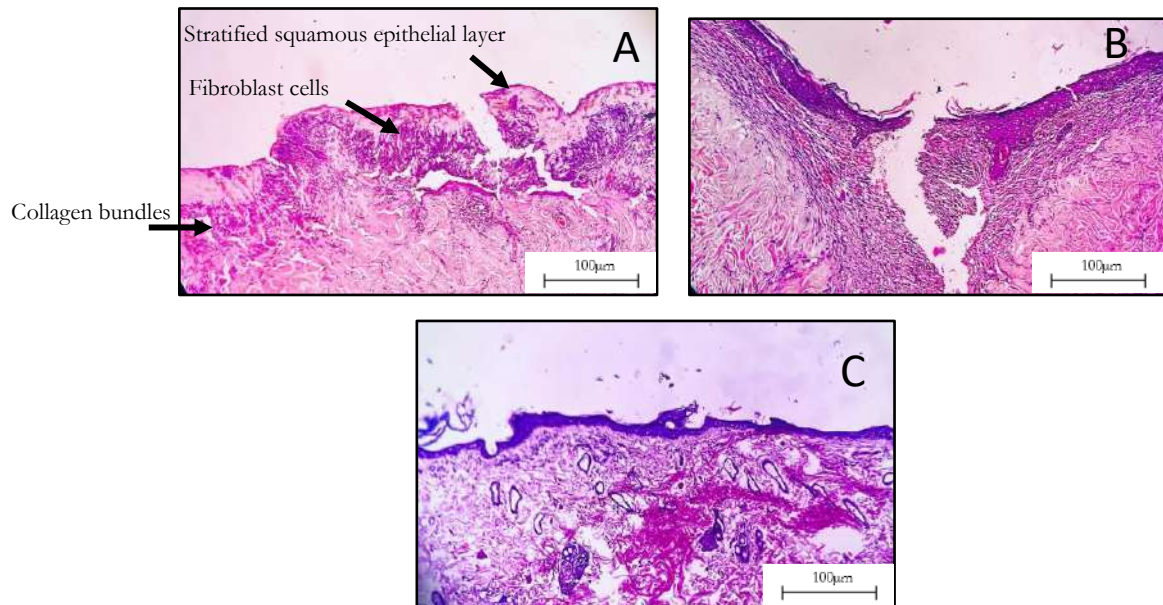
Figure 11 Images for H and E staining of (A) negative control group, (B) positive control and (C)TNF with AgNPs. Group A) shows re-epithelization of the stratified squamous epithelium with angiogenesis, Group B) shows maturation of re-epithelization of the stratified squamous epithelium with multifocal area of proliferation of, formation thin and thick bundles of collagen Group C) shows complete re-epithelization of the stratified squamous epithelium, with proliferation of fibroblast, homogenous deposition of thin and thick collagen bundles with angiogenesis.

In addition, the wound site's collagen deposition (blue) was evaluated using Masson's Trichrome staining (Figure 12). Figure 12 A shows that there was initiation of formation of thin and thick bundle of collagen fibres with no inflammatory cells, it showed the presence of collagen (blue), probably because of the presence fibroblast cells and the collagen deposition was scanty and still in nascent stages which indicated that the wound was at proliferation phase, which was complimentary to the results of the H and E staining. While Figure 12 B showed complete maturation of collagen fibres, and more pronounced and homogenous collagen deposition was observed, with highest collagen deposition along with the formation of myofibroblast formation at the wound site. In comparison to the open wound and the wound treated with gauze, the wound treated with AgNPs loaded TNF (Figure 12 C) showed lower collagen content at the wound area, which might be due to more mature collagen formation and more hair follicles being regenerated, additionally formation of muscle tissue (red) was also observed which also indicated the initiation of the remodelling phase [75]. Thus, overall, the study confirmed that the novel TNF dressing containing AgNPs could be a promising candidate for wound healing applications, as an ''all-in-one'' solution
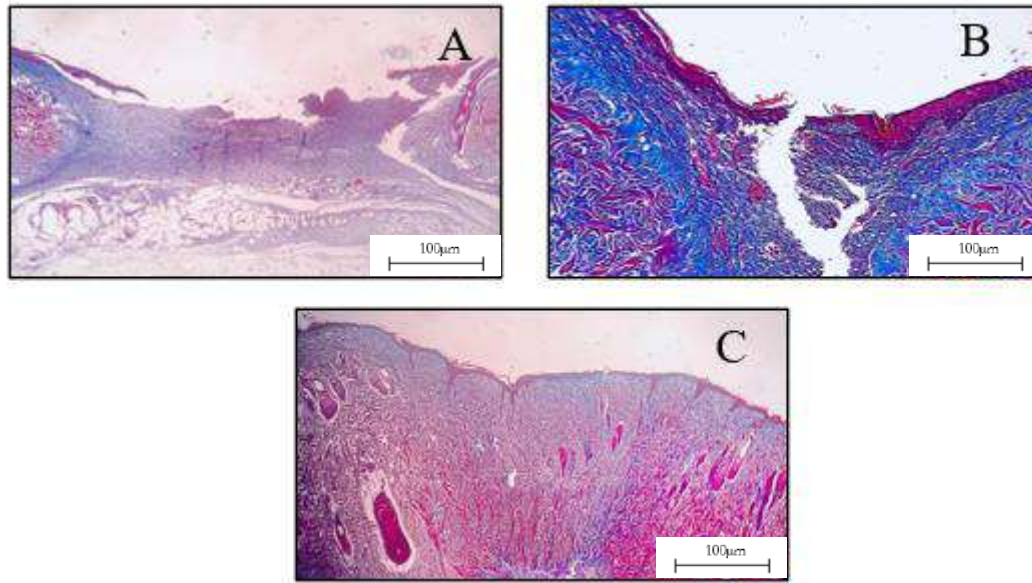
Figure 12 Images for Masson's Trichrome staining of (A) negative control group, (B) positive control, and (C)TNF with AgNPs. Group A) shows the formation of thin and thick bundles of collagen fibers with no inflammatory cells Group B) shows complete maturation of collagen fibers, and more pronounced and homogenous collagen deposition Group C) shows mature collagen formation and more hair follicles

6.0 Conclusion

In conclusion, we have fabricated a highly biocompatible, hemocompatible, biodegradable, antibacterial, atraumatic nanoengineered triple-layered wound dressing bandage to exhibit multiple healing functions. The top-most PVA CA layer was able to prevent dehydration and provide excellent mechanical strength to the middle therapeutic layer. The middle layer, loaded with AgNPs, showed controlled drug release. Use of CEA in the middle layer resulted in controlled water uptake, vapor evaporation to maintain moist environment at the wound site by absorbing and retaining wound exudates, and promoted excellent oxygen permeability and fluid drainage to speed up wound healing. While the PCL layer resulted in better adhesion to the skin cells and exhibited potential to avoid painful removal. The NF mats demonstrated highly effective antibacterial activity against Gram-positive *(S. aureus)* and Gram-negative *(E. coli)* bacteria; additionally, the porous structure of the PCL layer may mimic the properties of the skin's extracellular matrix. The potential of the nanofibrous mat in full-thickness wound healing was further confirmed by H&E, Masson's trichrome staining and in vivo excisional wound contraction. Thus, a triple layered AgNPs loaded PVA/CEA/PCL nanofibrous mat acted as a multi-functional dressing to accelerate wound healing and also demonstrated potential for other tissue engineering applications.

7.0 Future work:

In aforesaid mentioned pre-clinical studies to investigate wound healing efficacy, we have used traditional dressing i.e. cotton gauze to compare with triple-layered fabricated dressing. However, after completion of these studies we have come to know that, there are modern microfiber-based dressings are clinically available. Henceforth, before going for a clinical trial setting, we have decided to extend our preclinical studies for a comparison of wound healing efficacy of fabricated nanofiber dressing with a comparison with modern microfiber-based dressing i.e. Maxiocel from Axio BioSolutions, we have submitted form B to the IAEC committee for the same.

8.0 Impact of the research in the advancement of knowledge or benefit to mankind

The complex process of wound healing comprises of coagulation and homeostasis, inflammation, migration, proliferation, and maturation phase. However, obstruction of this process at any stage may result in the formation of chronic wounds. Chronic wounds can present a huge challenge to effectively heal. Currently, there are several biomaterial-based wound dressings available for healing diverse types of wounds. However, commercial wound-care dressings are too expensive to be affordable to the populations belonging to the middle and lower-socioeconomic strata. Hence, the major challenge is not only to develop an effective wound-care dressing that has better/comparable efficacy to the existing ones, but also to reduce the pain associated with the repeated changing of dressings in case of chronic wounds and also provide a cost-effective product to the patients. The novel multifunctional dressing developed for the treatment of chronic wounds has been designed to offer the following benefits:

1. Enhanced wound healing: The advanced wound dressing can promote faster and more effective wound closure, reducing recovery time.
2. Improved quality of life: Chronic wounds can significantly impact daily life; our dressing will alleviate pain, discomfort, and distress associated with multiple dressing changes.
3. Reduced healthcare costs: The use of synthetic, relatively low-cost, yet pharmaceutically approved polymers, along with versatile and easy-to-scale-up technology, will help to ultimately reduce the cost of wound dressing. Also faster and more effective wound healing can reduce the hospitalization time of the patients and also the associated costs.
4. Minimized scarring: Developed dressing will promote tissue regeneration, reducing scarring and improve cosmetic outcomes.
5. Reduced risk of infection: Due to the anti-microbial properties of the dressing, it will reduce risk of deadly infections and reduce patient morbidity.
6. Enhanced patient compliance: The developed atraumatic dressings can reduce the pain associated with repeated changing of the dressings and thus enhance the comfort and acceptance of the patients for the treatment
7. Advancements in medical technology: Developed triple-layered dressing is based on an innovative design, with each component individually contributing to wound healing, thus pushing the boundaries of medical technology and improving patient care.

Thus, by addressing the complex challenges of healing chronic wounds, the said dressing can significantly improve and save lives of sizeable patient-population nationwide, enhancing their

well-being, mobility, and overall quality of life, especially of those from the middle and lower socioeconomic strata of the society.

9.0 Acknowledgement:

10.0 Literature References:

1. Zhong, J., et al., *Reversibly immortalized keratinocytes (iKera) facilitate re-epithelization and skin wound healing: Potential applications in cell-based skin tissue engineering.* Bioactive Materials, 2022. **9**: p. 523-540.
2. Pereira, R.F., et al., *Advances in bioprinted cell-laden hydrogels for skin tissue engineering.* Biomanufacturing Reviews, 2017. **2**: p. 1-26.
3. Hao, R., et al., *Rational design and preparation of functional hydrogels for skin wound healing.* Frontiers in Chemistry, 2022. **9**: p. 839055.
4. Guo, S.a. and L.A. DiPietro, *Factors affecting wound healing.* Journal of dental research, 2010. **89**(3): p. 219-229.
5. Jones, V., J.E. Grey, and K.G. Harding, *Wound healing: a cellular perspective*

Bmj, 2006. **332**(7544): p. 777-780.
6. Kong, D., et al., *Adhesion loss mechanism based on carboxymethyl cellulose-filled hydrocolloid dressings in physiological wounds environment.* Carbohydrate polymers, 2020. **235**: p. 115953.
7. Kim, H.S., et al., *Advanced drug delivery systems and artificial skin grafts for skin wound healing.* Advanced drug delivery reviews, 2019. **146**: p. 209-239.
8. Zhao, Y., et al., *Preparation of nanofibers with renewable polymers and their application in wound dressing.* International Journal of Polymer Science, 2016. **2016**.
9. Choudhury, H., et al., *Silver nanoparticles: Advanced and promising technology in diabetic wound therapy.* Materials Science and Engineering: C, 2020. **112**: p. 110925.
10. Zhang, Q., et al., *Electrospun polymeric micro/nanofibrous scaffolds for long-term drug release and their biomedical applications.* Drug Discovery Today, 2017. **22**(9): p. 1351-1366.
11. Varesano, A., R.A. Carletto, and G. Mazzuchetti, *Experimental investigations on the multi-jet electrospinning process.* Journal of Materials Processing Technology, 2009. **209**(11): p. 5178-5185.
12. Nirwan, V.P., et al., *Advances in electrospun hybrid nanofibers for biomedical applications.* Nanomaterials, 2022. **12**(11): p. 1829.
13. Rieger, K.A., N.P. Birch, and J.D. Schiffman, *Designing electrospun nanofiber mats to promote wound healing–a review.* Journal of Materials Chemistry B, 2013. **1**(36): p. 4531-4541.
14. Hu, X., et al., *Electrospinning of polymeric nanofibers for drug delivery applications.* Journal of controlled release, 2014. **185**: p. 12-21.
15. Lim, C.T., *Nanofiber technology: current status and emerging developments.* Progress in polymer science, 2017. **70**: p. 1-17.

16. Khan, M.Q., et al., *Fabrication of antibacterial electrospun cellulose acetate/silver-sulfadiazine nanofibers composites for wound dressings applications.* Polymer Testing, 2019. **74**: p. 39-44.

17. Dabiri, G., E. Damstetter, and T. Phillips, *Choosing a wound dressing based on common wound characteristics.* Advances in wound care, 2016. **5**(1): p. 32-41.

18. Gorain, B. and S.P. Sisinthy, *Delivery of therapeutics from layer-by-layer electrospun nanofiber matrix for wound healing: An update.*

19. Tort, S., F. Acartürk, and A. Beşikci, *Evaluation of three-layered doxycycline-collagen loaded nanofiber wound dressing.* International Journal of Pharmaceutics, 2017. **529**(1-2): p. 642-653.

20. Natarajan, V., et al., *Preparation and properties of tannic acid cross-linked collagen scaffold and its application in wound healing.* Journal of Biomedical Materials Research Part B: Applied Biomaterials, 2013. **101**(4): p. 560-567.

21. Helary, C., et al., *Evaluation of dense collagen matrices as medicated wound dressing for the treatment of cutaneous chronic wounds.* Biomaterials science, 2015. **3**(2): p. 373-382.

22. Kamoun, E.A., E.-R.S. Kenawy, and X. Chen, *A review on polymeric hydrogel membranes for wound dressing applications: PVA-based hydrogel dressings.* Journal of advanced research, 2017. **8**(3): p. 217-233.

23. Chen, Q. and K. Zhou, *Acetic acid use in chronic wound healing: a multiple case series.* Journal of Wound Ostomy & Continence Nursing, 2022. **49**(3): p. 286-289.

24. Liu, X., et al., *Antimicrobial electrospun nanofibers of cellulose acetate and polyester urethane composite for wound dressing.* Journal of Biomedical Materials Research Part B: Applied Biomaterials, 2012. **100**(6): p. 1556-1565.

25. Fahimirad, S. and M. Ghorbanpour, *Omics approaches in developing abiotic stress tolerance in rice (Oryza sativa L.)*, in *Advances in rice research for abiotic stress tolerance.* 2019, Elsevier. p. 767-779.

26. Do Pham, D.D., et al., *Novel lipophosphonoxin-loaded polycaprolactone electrospun nanofiber dressing reduces Staphylococcus aureus induced wound infection in mice.* Scientific reports, 2021. **11**(1): p. 17688.

27. Balcucho, J., D.M. Narváez, and J.L. Castro-Mayorga, *Antimicrobial and biocompatible polycaprolactone and copper oxide nanoparticle wound dressings against methicillin-resistant Staphylococcus aureus.* Nanomaterials, 2020. **10**(9): p. 1692.

28. Asiri, A., et al., *Epidermal and fibroblast growth factors incorporated polyvinyl alcohol electrospun nanofibers as biological dressing scaffold.* Scientific reports, 2021. **11**(1): p. 5634.

29. Nataraj, D., R. Reddy, and N. Reddy, *Crosslinking electrospun poly (vinyl) alcohol fibers with citric acid to impart aqueous stability for medical applications.* European Polymer Journal, 2020. **124**: p. 109484.

30. Katsogiannis, K.A.G., G.T. Vladisavljević, and S. Georgiadou, *Porous electrospun polycaprolactone (PCL) fibres by phase separation.* European Polymer Journal, 2015. **69**: p. 284-295.

31. Pandey, G., et al., *Multilayered nanofibrous scaffold of Polyvinyl alcohol/gelatin/poly (lactic-co-glycolic acid) enriched with hemostatic/antibacterial agents for rapid acute hemostatic wound healing.* International journal of pharmaceutics, 2023. **638**: p. 122918.

32. Lin, W., et al., *Near-Infrared Light-Responsive Nanofibrous Membranes for Treatment of Bacterial Wound Infections.* ACS Applied Nano Materials, 2023. **6**(21): p. 20298-20309.

33. Nangare, S., et al., *Silk industry waste protein: isolation, purification and fabrication of electrospun silk protein nanofibers as a possible nanocarrier for floating drug delivery.* Nanotechnology, 2020. **32**(3): p. 035101.

34. Hankiewicz, J. and E. Swierczek, *Lysozyme in human body fluids.* Clinica chimica acta, 1974. **57**(3): p. 205-209.

35. Waghmare, V.S., et al., *Starch based nanofibrous scaffolds for wound healing applications.* Bioactive materials, 2018. **3**(3): p. 255-266.

36. Mistry, P., et al., *Fabrication and characterization of starch-TPU based nanofibers for wound healing applications.* Materials Science and Engineering: C, 2021. **119**: p. 111316.

37. Wadke, P., et al., *Silver-embedded starch-based nanofibrous mats for soft tissue engineering.* Surfaces and Interfaces, 2017. **8**: p. 137-146.

38. Feng, Y., et al., *Antibiofouling zwitterionic gradational membranes with moisture retention capability and sustained antimicrobial property for chronic wound infection and skin regeneration.* Biomacromolecules, 2019. **20**(8): p. 3057-3069.

39. Vashisth, P. and V. Pruthi, *Synthesis and characterization of crosslinked gellan/PVA nanofibers for tissue engineering application.* Materials Science and Engineering: C, 2016. **67**: p. 304-312.

40. Wu, S., et al., *Improving the water resistance and mechanical properties of feather keratin/polyvinyl alcohol/tris (hydroxymethyl) aminomethane blend films by cross-linking with transglutaminase, cacl2, and genipin.* Materials, 2018. **11**(11): p. 2203.

41. Samnani, M., H. Rathod, and H. Raval, *A novel reverse osmosis membrane modified by polyvinyl alcohol with maleic anhydride crosslinking.* Materials Research Express, 2018. **5**(3): p. 035304.

42. Rudra, R., V. Kumar, and P.P. Kundu, *Acid catalysed cross-linking of poly vinyl alcohol (PVA) by glutaraldehyde: effect of crosslink density on the characteristics of PVA membranes used in single chambered microbial fuel cells.* RSC advances, 2015. **5**(101): p. 83436-83447.

43. Gyawali, D., et al., *Citric acid-derived in situ crosslinkable biodegradable polymers for cell delivery.* Biomaterials, 2010. **31**(34): p. 9092-9105.

44. Sekar, A.D., et al., *Electrospinning of Fe-doped ZnO nanoparticles incorporated polyvinyl alcohol nanofibers for its antibacterial treatment and cytotoxic studies.* European Polymer Journal, 2019. **118**: p. 27-35.

45. Wilpiszewska, K., A.K. Antosik, and M. Zdanowicz, *The effect of citric acid on physicochemical properties of hydrophilic carboxymethyl starch-based films.* Journal of Polymers and the Environment, 2019. **27**: p. 1379-1387.

46. Xiao, W., et al., *Antibacterial hybrid materials fabricated by nanocoating of microfibril bundles of cellulose substance with titania/chitosan/silver-nanoparticle composite films.* Journal of Materials Chemistry B, 2013. **1**(28): p. 3477-3485.

47. Augustine, R., N. Kalarikkal, and S. Thomas, *Effect of zinc oxide nanoparticles on the in vitro degradation of electrospun polycaprolactone membranes in simulated body fluid.* International Journal of Polymeric Materials and Polymeric Biomaterials, 2016. **65**(1): p. 28-37.

48. Reguieg, F., et al., *Thermal characterization by DSC and TGA analyses of PVA hydrogels with organic and sodium MMT.* Polymer Bulletin, 2020. **77**(2): p. 929-948.

49. Poh, C.K., et al., *Citric acid functionalized carbon materials for fuel cell applications.* Journal of power sources, 2008. **176**(1): p. 70-75.

50. Barud, H.S., et al., *Thermal behavior of cellulose acetate produced from homogeneous acetylation of bacterial cellulose.* Thermochimica acta, 2008. **471**(1-2): p. 61-69.

51.   Saeed, K., et al., *Preparation of electrospun nanofibers of carbon nanotube/polycaprolactone nanocomposite.* Polymer, 2006. **47**(23): p. 8019-8025.

52.   Patel, A.K., R. Bajpai, and J. Keller, *On the crystallinity of PVA/palm leaf biocomposite using DSC and XRD techniques.* Microsystem technologies, 2014. **20**: p. 41-49.

53.   Mei, J.-Q., et al., *Effects of citric acid esterification on digestibility, structural and physicochemical properties of cassava starch.* Food Chemistry, 2015. **187**: p. 378-384.

54.   Prakash, J., et al., *In-vitro evaluation of electrospun cellulose acetate nanofiber containing Graphene oxide/TiO2/Curcumin for wound healing application.* Colloids and Surfaces A: Physicochemical and Engineering Aspects, 2021. **627**: p. 127166.

55.   Zeng, W., et al., *Electrospun polycaprolactone nanofibrous membranes loaded with baicalin for antibacterial wound dressing.* Scientific Reports, 2022. **12**(1): p. 10900.

56.   Chen, G., T. Ushida, and T. Tateishi, *Development of biodegradable porous scaffolds for tissue engineering.* Materials Science and Engineering: C, 2001. **17**(1-2): p. 63-69.

57.   Liang, H., et al., *Fabrication of tragacanthin gum-carboxymethyl chitosan bio-nanocomposite wound dressing with silver-titanium nanoparticles using freeze-drying method.* Materials Chemistry and Physics, 2022. **279**: p. 125770.

58.   Zaman, H.U., et al., *Physico-mechanical properties of wound dressing material and its biomedical application.* Journal of the mechanical behavior of biomedical materials, 2011. **4**(7): p. 1369-1375.

59.   Tavakoli, J. and Y. Tang, *Honey/PVA hybrid wound dressings with controlled release of antibiotics: Structural, physico-mechanical and in-vitro biomedical studies.* Materials Science and Engineering: C, 2017. **77**: p. 318-325.

60.   Kimna, C., S. Tamburaci, and F. Tihminlioglu, *Novel zein-based multilayer wound dressing membranes with controlled release of gentamicin.* Journal of Biomedical Materials Research Part B: Applied Biomaterials, 2019. **107**(6): p. 2057-2070.

61.   Xu, R., et al., *Controlled water vapor transmission rate promotes wound-healing via wound re-epithelialization and contraction enhancement.* Scientific reports, 2016. **6**(1): p. 24596.

62.   Razavi, S.Z., et al., *Polycaprolactone/cress seed mucilage based bilayer antibacterial films containing ZnO nanoparticles with superabsorbent property for the treatment of exuding wounds.* International Journal of Biological Macromolecules, 2024. **256**: p. 128090.

63.   Karimi, M., et al., *Fabrication of shapeless scaffolds reinforced with baghdadite-magnetite nanoparticles using a 3D printer and freeze-drying technique.* Journal of Materials Research and Technology, 2021. **14**: p. 3070-3079.

64.   Barua, B. and M.C. Saha, *Influence of humidity, temperature, and annealing on microstructure and tensile properties of electrospun polyacrylonitrile nanofibers.* Polymer Engineering & Science, 2018. **58**(6): p. 998-1009.

65.   Itoh, H., et al., *Morphology and mechanical properties of PVA nanofibers spun by free surface electrospinning.* Polymer Bulletin, 2016. **73**: p. 2761-2777.

66.   Eskandarinia, A., et al., *A propolis enriched polyurethane-hyaluronic acid nanofibrous wound dressing with remarkable antibacterial and wound healing activities.* International journal of biological macromolecules, 2020. **149**: p. 467-476.

67.   Eskandarinia, A., et al., *A novel bilayer wound dressing composed of a dense polyurethane/propolis membrane and a biodegradable polycaprolactone/gelatin nanofibrous scaffold.* Scientific reports, 2020. **10**(1): p. 3063.

68.   Dharavath, D. and R. Maddi, *ISO standards of medical devices.* World Journal of Current Medical and Pharmaceutical Research, 2022: p. 33-39.

1309 69. O'brien, J., et al., *Investigation of the Alamar Blue (resazurin) fluorescent dye for the*
1310   *assessment of mammalian cell cytotoxicity.* European journal of biochemistry, 2000.
1311   **267**(17): p. 5421-5426.
1312 70. Ong, S.-Y., et al., *Development of a chitosan-based wound dressing with improved*
1313   *hemostatic and antimicrobial properties.* Biomaterials, 2008. **29**(32): p. 4323-4332.
1314 71. Dugam, S., et al., *Crystallinity modulated silk fibroin electrospun nanofibers based*
1315   *floating scaffold as a candidate for controlled release of felodipine.* International
1316   Journal of Polymeric Materials and Polymeric Biomaterials, 2022. **71**(18): p. 1393-
1317   1406.
1318 72. Lee, S.H. and B.-H. Jun, *Silver nanoparticles: synthesis and application for*
1319   *nanomedicine.* International journal of molecular sciences, 2019. **20**(4): p. 865.
1320 73. Ansari, M.A., et al., *Interaction of silver nanoparticles with Escherichia coli and their*
1321   *cell envelope biomolecules.* Journal of basic microbiology, 2014. **54**(9): p. 905-915.
1322 74. Chhabra, R., et al., *In vivo studies of 3D starch–gelatin scaffolds for full-thickness*
1323   *wound healing.* ACS Applied Bio Materials, 2020. **3**(5): p. 2920-2929.
1324 75. Xie, Z., et al., *Dual growth factor releasing multi-functional nanofibers for wound*
1325   *healing.* Acta biomaterialia, 2013. **9**(12): p. 9351-9359.

1326
1327
1328
1329
1330
1331

1332 Shailesh Dugam
1333 Ph. D Research Scholar (DST Inspire- Senior Research Fellow)
1334 Department of Pharmaceutical Sciences and Technology,
1335 Institute of Chemical Technology,
1336 Matunga, Mumbai -400019

Supporting Information:

Silver nanoparticles were inhouse synthesized using unique micellar technology. 10mM of $AgNO_3$ and 3 mM of $NaBH_4$ were used for formulation of silver nanoparticles. Herein, $NaBH_4$ was used as the reducing agent and poly ethylene glycol (PEG) was used as the capping agent. The method for formulation for silver nanoparticles was optimized for process parameters like residence time (sec), flow Rate of $AgNO_3$ (µL/min), flow Rate of $NaBH_4$ (µL/min) flow ratio of $AgNO_3$ and $NaBH_4$. The details of optimization parameters for development of silver nanoparticles depicted in Table S1, S2, S3 and S4 and for optimization of capping agent is depicted in Table 2. During optimization, silver nanoparticle was preliminary analyzed using zetasizer nano ZSP (Malvern Instruments Ltd., Worcestershire, UK) for its size and polydispersity index. An average of three runs was considered while reporting the size and polydispersity index. The prepared silver nanoparticles with optimized parameters were further characterized using UV-spectroscopy (UV-2600, Shimadzu, Japan) and TEM (FEI Tecnai 12, Netherlands) at an acceleration voltage of 200 kV.

Table S1: Optimization of Microreactor Parameters for Development of Silver nanoparticles

(Flow ratio $AgNO_3$: $NaBH_4$, 1:1)

Residence Time (sec)	Flow rate of AgNO3 (µL/min)	Flow Rate of NaBH4 (µL/min)	Size of AgNPs (nm)	Polydispersity Index (PDI)
0.5 sec	2700	2700	52.99±0.7789	0.88
1 sec	1350	1350	36.54±0.59	0.657
1.5 sec	900	900	36.39±0.65	0.637

Table S2: Optimization of Microreactor Parameters for Development of Silver nanoparticles

(Flow ratio $AgNO_3$: $NaBH_4$, 1:5)

Residence Time (sec)	Flow Rate of $AgNO_3$(µL/min)	Flow Rate of $NaBH_4$ (µL/min)	Size of AgNPs (nm)	Polydispersity Index (PDI)
0.5 sec	900	4500	36.38±0.6070	0.768
1 sec	450	2250	32.45±0.2023	0.590
1.5 sec	300	1500	36.74±0.675	0.675

Table S3: Optimization of Microreactor Parameters for Development of Silver nanoparticles

(Flow ratio AgNO$_3$: NaBH$_4$, 1:10)

Residence Time (sec)	Flow Rate of AgNO$_3$ (μL/min)	Flow Rate of NaBH$_4$ (μL/min)	Size of AgNPs (nm)	Polydispersity Index (PDI)
0.5 sec	490	4909.90	15.67±0.595	0.595
1 sec	245	2454.45	14.41±0.4382	0.622
1.5 sec	163.6	1636.66	15.49±0.626	0.626

Table S4) Optimization for concentration of stabilizing agent (PEG) for formulation of silver nanoparticle

Conc. of PEG (% w with respect to weight of AgNO$_3$)	Flow ratio (AgNO$_3$: NaBH$_4$)	Residence Time (sec)	Flow Rate of AgNO$_3$ (μL/min)	Flow Rate of NaBH$_4$ (μL/min)	Size of AgNPs (nm)	Polydispersity Index (PDI)
10%	1:10	0.5	490	4909.90	27.45±0.9681	0.63
15%	1:10	0.5	490	4909.90	15.67±0.9771	0.595
20%	1.:10	0.5	490	4909.90	24.10±0.4382	0.414

The optimized process parameters like flow ratio (AgNO$_3$: NaBH$_4$ (1:10) , with residence time 0.5 sec, having 20% concentration of stabilizing agent formulate smaller and uniformly distributed silver nanoparticles
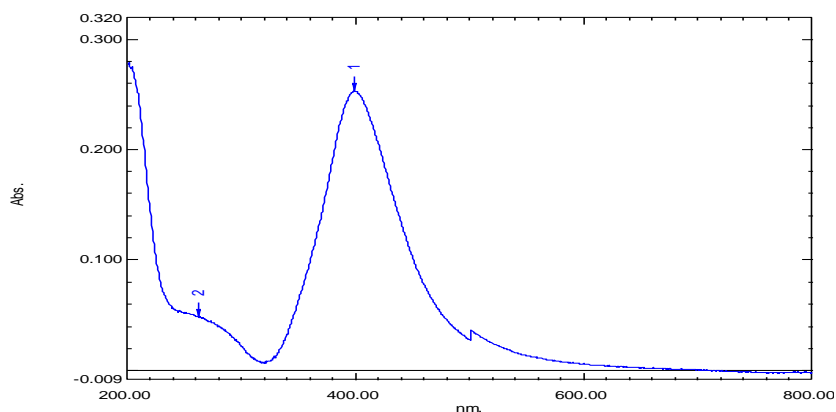
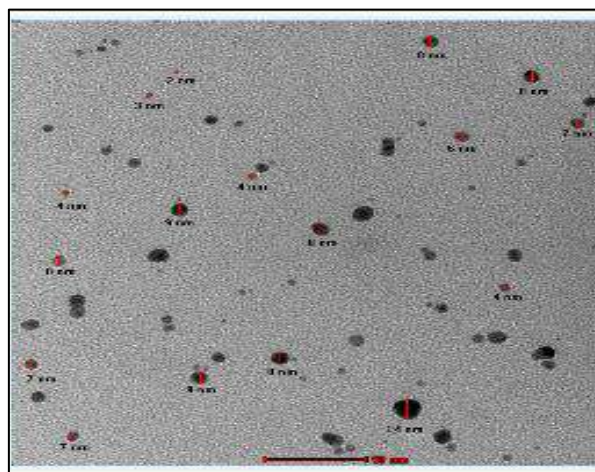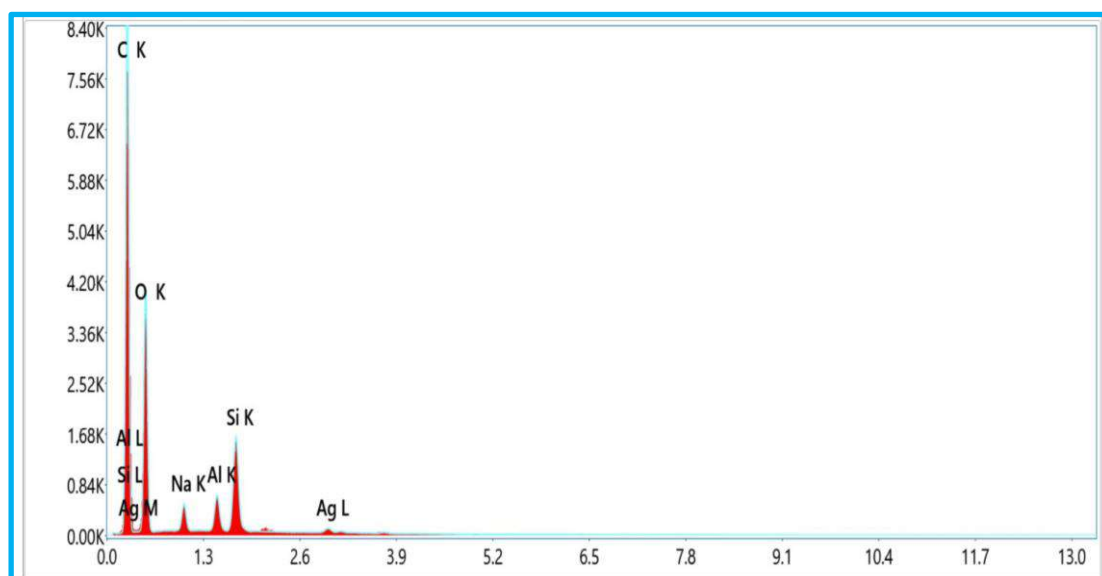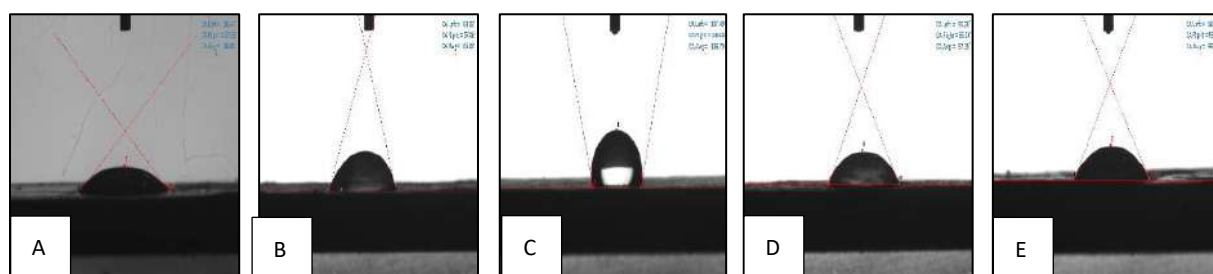Figure S1: UV-visible spectra of Silver nanoparticles

Figure S2) TEM images of AgNPs

Figures S3) . EDAX spectra for AgNPs loaded CEA NF sheet

Figures S4) Water contact angle for PVA, PVA CA NF, CEA NF, PCL NF and TNF